

# On effects of resolution in dissipationless cosmological simulations

Alexander Knebe,<sup>1,2</sup> Andrey V. Kravtsov,<sup>3,4</sup> Stefan Gottlöber<sup>1</sup>  
and Anatoly A. Klypin<sup>3</sup>

<sup>1</sup> *Astrophysikalisches Institut Potsdam (AIP), An der Sternwarte 16, 14482 Potsdam, Germany*

<sup>2</sup> *Theoretical Physics, 1 Keble Road, Oxford OX1 3NP, UK*

<sup>3</sup> *Astronomy Department, New Mexico State University, Dept. 4500, Las Cruces, NM 88003-0001, USA*

<sup>4</sup> *Current address: Department of Astronomy, The Ohio State University, 140 W. 18th Ave., Columbus, OH 43210-1173, USA*

Received ...; accepted ...

## ABSTRACT

We present a study of numerical effects in dissipationless cosmological simulations. The numerical effects are evaluated and studied by comparing results of a series of  $64^3$ -particle simulations of varying force resolution and number of time steps, performed using three of the  $N$ -body techniques currently used for cosmological simulations: the Particle Mesh (PM), the Adaptive Particle-Particle Particle-Mesh (AP<sup>3</sup>M), and the newer Adaptive Refinement Tree (ART) code. This study can therefore be interesting both as an analysis of numerical effects and as a systematic comparison of different codes.

We find that the AP<sup>3</sup>M and the ART codes produce similar results, given that convergence is reached within the code type. We also find that numerical effects may affect the high-resolution simulations in ways that have not been discussed before. In particular, our study revealed the presence of two-body scattering, effects of which can be greatly amplified by inaccuracies of time integration. This process appears to affect the correlation function of matter, mass function and inner density of dark matter halos and other statistics at scales much larger than the force resolution, although different statistics may be affected in different fashion. We discuss the conditions at which strong two-body scattering is possible and discuss the choice of the force resolution and integration time step. Furthermore, we discuss recent claims that simulations with force softening smaller than the mean interparticle separation are not trustworthy and argue that this claim is incorrect in general and applies only to the phase-sensitive statistics. Our conclusion is that, depending on the choice of mass and force resolution and integration time step, a force resolution as small as 0.01 of the mean interparticle separation can be justified.

**Key words:** cosmology – numerical simulations.

## 1 INTRODUCTION

Dissipationless cosmological  $N$ -body simulations are currently the tool of choice for following the evolution of cold dark matter (CDM) into the highly nonlinear regime. For the widest range of plausible dark matter (DM) candidates (from axions of mass  $\sim 10^{-6} - 10^{-3}$  eV to  $\sim 10^{21} - 10^{25}$  eV wimpzillas; see, e.g., Kolb, Chung & Riotto 1998; Roszkowski 1999), their expected number density is  $n_{\text{DM}} \sim (10^{52} - 10^{83})\Omega_0 h^2 \text{ Mpc}^{-3}$ .  $N$ -body simulations numerically solve the  $N$ -body problem: given initial positions and velocities for  $N$  pointlike massive objects, the simulations predict the particle positions and velocities at any subsequent time. Current  $N$ -body simulations

are capable of following the evolution of  $\lesssim 10^9$  particles, far short of the expected number of DM particles. Therefore, the correct approach to modelling dark matter evolution in a cosmologically representative volume, is to use the Vlasov equation (collisionless Boltzmann equation) coupled with the Poisson equation and complemented by appropriate boundary conditions. However, a full-scale modelling of 6D distribution functions with reasonable spatial resolution is extremely challenging computationally. The alternative approach adopted in most cosmological simulations is to split the initial phase space into small volume elements and follow evolution of these elements using  $N$ -body techniques. Each volume element can thus be thought of as an  $N$ -body

particle, which moves with a flow and which has some shape (for example, a box or a sphere) or is simply point-like. Two particles are assumed to interact gravitationally only if they are separated by a distance  $\gtrsim \epsilon$ , where  $\epsilon$  is the *smoothing scale*, often referred to as the *force resolution*. It is clear that the “size” of a particle is determined by the eulerian spatial size of the initial phase space volume element or by the smoothing scale, whichever is smaller.

While this approach seems logical and reasonable and is expected to provide approximate solution to a complicated problem, questions of its limitations may be raised. For example, while particle shape is usually considered to be rigid (fixed by a specific form of the Green function or the shape of the interparticle force), in eulerian space the shape of the initially cubic phase space volume element can be expected to be stretched as the element moves towards higher density regions. Its volume can also change so as to preserve the phase space density. Furthermore, under certain conditions the  $N$ -body systems may exhibit scattering, which is undesirable when one models a purely collisionless system. This may occur in cosmological simulations if the “size” of particles is much smaller than the *eulerian* spatial size of the phase space element they are supposed to represent.

These effects may influence the accuracy of the simulations and lead to spurious results. Nevertheless, surprisingly little attention has been given to studies of such limitations in the cosmological simulations. As the resolution of simulations improves and the range of their applications broaden, it becomes increasingly important to address these issues. Indeed, during the past decade the force resolution of the simulations has improved by a factor of  $\sim 100 - 1000$ , while (with rare exceptions) the mass resolution has improved only by a factor of  $\sim 10$ . Also, modern high-resolution codes follow evolution of cosmological systems for many dynamical time-scales. In this regime the accuracy of the force estimates may be less important than the stability of the overall solution. These issues are usually not addressed when tests of codes are presented.

Recently, in a series of papers Melott and collaborators (Kuhlman, Melott & Shandarin 1996; Melott et al. 1997; Splinter et al. 1998) raised the issue of the balance between the force and the mass resolution. While we disagree with their main conclusion that the force resolution should be larger than the mean interparticle separation (see § 3 and § 5), we agree that the issue is important.

There is also a common misconception related to the adaptive mesh refinement approach in cosmological simulations and other algorithms that integrate equations of particle motion in *comoving* coordinates. The common criticism (e.g., Splinter et al. 1998 and references therein) is that these algorithms attempt to resolve scales unresolved in the initial conditions (the scales below approximately half of the Nyquist frequency). However, the goal of increasing the resolution in comoving coordinates is not to resolve the waves not present in the initial conditions but rather to properly follow all of the waves initially present.

When followed in comoving coordinates, gravitational instability leads to the separation of structures from the Hubble flow and collapse, resulting in the transfer of power to higher wavenumbers. If the force resolution is fixed in *comoving* coordinates at the Nyquist frequency of the initial conditions, this transfer cannot be modelled properly

for all waves. Moreover, the size of structures that have collapsed and virialized stays fixed in the proper coordinates and decreases in comoving coordinates. When the comoving size of such objects becomes smaller than the resolution of a fixed grid simulation, their subsequent evolution and internal properties will be modelled incorrectly. Adaptive mesh refinement algorithms address this problem by increasing the force resolution locally to follow the evolution of collapsing and virialized density peaks as their size becomes less than the resolution of the original grid. Other algorithms can achieve the same result by varying the comoving force softening with time.

Our motivation for the present study is twofold. Our first goal is to elaborate on the issue of spurious numerical effects. Namely, we study the effects of the balance of force and mass resolutions and of time integration details on statistics commonly used in analyses of cosmological simulations. The balance of force and mass resolutions should be studied by varying both of the resolutions. In this study, however, we will keep the mass resolution fixed and vary the force resolution instead. While this may not reveal all of the artificial effects<sup>\*</sup>, this allows to study the spurious two-body scattering present when the smoothing scale is set to be too small. It also allows us to study how the limited force resolution affects various statistical properties of the dark matter distribution. Our second goal is to compare results produced using two of the currently employed high-resolution  $N$ -body codes: AP<sup>3</sup>M (Couchman 1991) and ART (Kravtsov, Klypin & Khokhlov 1997). The comparison is of interest due to a relative novelty of the latter technique and some disagreement between the results concerning the details of the central density distribution in DM halos obtained using different codes (e.g., Moore 1994; Navarro, Frenk & White 1997; Kravtsov et al. 1998; Moore et al. 1999). This study can also be interesting as an independent test of the widely used AP<sup>3</sup>M code, for which virtually no systematic tests have been published to date.

The paper is organized as follows. In §2 we describe the  $N$ -body algorithms used in our study and describe the numerical simulations performed. In §3 we compare the dark matter distribution simulated using different codes with different force resolutions and time steps. In §4 we use these simulations to compare the properties and distribution of dark matter halos (dense virialized systems). In §5 we summarize the results of the code comparisons, discuss the effects of resolution and time step on the commonly used statistics, and present our conclusions.

## 2 COSMOLOGICAL $N$ -BODY SIMULATIONS

In this study we will use and compare three different  $N$ -body algorithms: Particle-Mesh (PM) algorithm (Hockney & Eastwood 1981), adaptive Particle-Particle Particle-Mesh algorithm (AP<sup>3</sup>M; Couchman 1991), and Adaptive Refinement Tree algorithm (ART; Kravtsov et al. 1997). The PM algorithm was first used for cosmological simulations by Doroshkevich et al. (1980), Efstathiou & Eastwood (1981),

<sup>\*</sup> For example, fixed mass resolution does not allow us to study the effects of the rigid particle shape mentioned above.

and Klypin & Shandarin (1983). The algorithm makes use of the fast Fourier transforms to solve the Poisson equation on a uniform grid and uses interpolation and numerical differentiation to obtain the force that acts on each particle.

The solution is limited by the number of particles (mass resolution) and by the size of the grid cell which defines force resolution. The exact shape of the resulting force depends on the specific form of the Green function and interpolation used to get the force. The technique is attractive due to its simplicity and the fact that it is numerically very robust. Highly efficient implementations have been developed and used during the past decade. The technique is described in detail by Hockney & Eastwood (1981) and we refer the reader to this book for further details. The specific implementations used in our study are those of the AP<sup>3</sup>M code and the ART code. The PM simulations presented here have been run using the publicly available AP<sup>3</sup>M code with the particle-particle part switched off and by the ART code with the mesh refinement block switched off. In the remainder of this section we will describe the AP<sup>3</sup>M and ART algorithms and the specifics of our test simulations.

## 2.1 AP<sup>3</sup>M Code

Particle-Particle-Particle-Mesh (P<sup>3</sup>M) codes (Hockney et al. 1973; Hockney & Eastwood 1981) express the inter-particle force as a sum of a short range force (computed by direct particle-particle pair force summation) and the smoothly varying part (approximated by the particle-mesh force calculation). One of the major problems for these codes is the correct splitting of the force into a short-range and a long-range part. The grid method (PM) is only able to produce reliable inter particle forces down to a minimum of at least two grid cells. For smaller separations the force can no longer be represented on the grid and therefore one must introduce a cut-off radius  $r_e$  (larger than two grid cells !) where for  $r < r_e$  the force should smoothly go to zero. The parameter  $r_e$  defines the chaining-mesh and for distances smaller than this cutoff radius  $r_e$  a contribution from the direct particle-particle (PP) summation needs to be added to the total force acting on each particle. Again this PP force should smoothly go to zero for very small distances in order to avoid unphysical particle-particle scattering. This cutoff of the PP force determines the overall force resolution of a P<sup>3</sup>M code.

The most widely used version of this algorithm is currently the adaptive P<sup>3</sup>M (AP<sup>3</sup>M) code of Couchman (1991). The smoothing of the force in this code is connected to a  $S_2$  sphere, as described in Hockney & Eastwood (1981). The particles are treated as density spheres with a profile

$$S_2 : \rho(r) = \begin{cases} \frac{48}{\pi\epsilon^4} \left( \frac{\epsilon}{2} - r \right), & \text{for } r < \epsilon/2 \\ 0, & \text{otherwise} \end{cases} \quad (1)$$

where  $\epsilon$  is the softening parameter. For distances greater than  $\epsilon$  the particles are treated as point masses interacting according to the newtonian  $1/r^2$  law, whereas for smaller separations the effective shape of the  $S_2$  sphere influences and modifies the force law such that the interaction drops down to zero as  $r \rightarrow 0$ .

When splitting the force into short- and long-range components, one has to use *two* softening parameters: one which

is directly connected to the cut-off radius  $r_e$  for the PM force and therefore tells us where to match the PM and PP part, and another which determines the overall force resolution (softening scale for PP force). The PP force is truncated at both the very low separations and at  $r \geq r_e$  where the force can be calculated using the mesh based PM method. The AP<sup>3</sup>M code uses a cut-off radius  $r_e$  for the long-range force of approximately 2.4 PM mesh cells, and this leads to the softening parameter of  $\epsilon_{\text{PM}} = 1.3r_e \approx 3.1$  (cf. Hockney & Eastwood 1981). The softening  $\epsilon$  of the PP force determines the overall force resolution; for the AP<sup>3</sup>M simulations presented in this paper the softening scales are given in Table 1. When setting the overall softening parameter to a value greater than 3.5 the code runs as a pure PM mesh based code, because the softening of the PP force is greater than that of the PM part.

Unfortunately, the particle-particle summation which allows one to achieve sub-grid resolutions and thereby makes the P<sup>3</sup>M algorithm attractive, is also the method's main drawback. The PP calculation must search for neighbors out to roughly two mesh spacings to properly augment the PM force. This becomes increasingly expensive as clustering develops and particles start to clump together (within the chaining-mesh cells). The adaptive P<sup>3</sup>M algorithm remedies this by covering the high-density, most computationally expensive regions with refinement grids. Within the refinements the direct sum is replaced by a further local P<sup>3</sup>M calculation with isolated boundary conditions performed on a finer refinement grid (PM mesh and chaining-mesh are refined). The number of particles per refinement grid cell is smaller and so is the PP associated computations. The number of grid cells per refinement depends on the total number of particles within that region, but is always a power of two. The criterion for placing a refinement depends only on the total number of particles inside a chaining-mesh cell. If this value exceeds a preselected threshold in a given region, the region is refined; for our runs we used a value of 50 particles. It is convenient to isolate patches which cover an exact cubic block of chaining-mesh cells. Recursively placed refinements are allowed, and in the simulations presented in this paper a maximum level of 3 was reached.

The AP<sup>3</sup>M code integrates equations of particle motion using  $p = a^{3/2}$  as a time variable (here  $a$  is the expansion factor; Efstathiou et al. 1985). A time-centered leapfrog integration with constant time step  $\Delta p$  is used. This scheme leads to "large" steps in  $a$  at the beginning of the simulation which then get progressively smaller during the course of simulation.

## 2.2 ART Code

The Adaptive Refinement Tree code (ART; Kravtsov et al. 1997) reaches high force resolution by refining all high-density regions with an automated refinement algorithm. The refinements are recursive: the refined regions can also be refined, each subsequent refinement having half of the previous level's cell size. This creates an hierarchy of refinement meshes of different resolutions covering regions of interest.

The refinement is done cell-by-cell (individual cells can be refined or de-refined) and meshes are not constrained to have a rectangular (or any other) shape. This allows the code to refine the required regions in an efficient manner. The

criterion for refinement is the *local overdensity* of particles: in the simulations presented in this paper the code refined an individual cell only if the density of particles (smoothed with the cloud-in-cell scheme; Hockney & Eastwood 1981) was higher than  $n_{th} = 5$  particles. Therefore, *all* regions with overdensity higher than  $\delta = n_{th} 2^{3L}/\bar{n}$ , where  $\bar{n}$  is the average number density of particles in the cube, were refined to the refinement level  $L$ . For the two ART simulations presented here,  $\bar{n} = 1/8$ . The Poisson equation on the hierarchy of meshes is solved first on the base grid and then on the subsequent refinement levels. On each refinement level the code obtains the potential by solving the Dirichlet boundary problem with boundary conditions provided by the already existing solution at the previous level. There is no particle-particle summation in the ART code and the actual force resolution is equal to  $\approx 2$  cells of the finest refinement mesh covering a particular region. A detailed description of the code, its tests, and discussion of the force shape is given in Kravtsov et al. (1997). Note, however, that the present version of the code uses multiple time steps on different refinement levels, as opposed to the constant time stepping in the original version of the code. The multiple time stepping scheme is described in some detail in Kravtsov et al. (1998; also see below).

The refinement of the time integration mimics spatial refinement and the time step for each subsequent refinement level is two times smaller than the step on the previous level. Note, however, that particles on the same refinement level move with the same step. When a particle moves from one level to another, the time step changes and its position and velocity are interpolated to appropriate time moments. This interpolation is first-order accurate in time, whereas the rest of the integration is done with the second-order accurate time centered leap-frog scheme. All equations are integrated with the expansion factor  $a$  as a time variable and the global time step hierarchy is thus set by the step  $\Delta a_0$  at the zeroth level (uniform base grid). The step on level  $L$  is then  $\Delta a_L = \Delta a_0/2^L$ .

The choice of an appropriate time step for a simulation is dictated by the peak force resolution. The number of time steps in our simulations is such that the *rms* displacement of particles during a single time-step is always less than 1/4 of a cell. No particles moves further than  $\sim 0.5$  cells in a single time step, where the cell size and time step for particles located on the refinement level  $L$  are  $\Delta x_0/2^L$  and  $\Delta a_0/2^L$ , respectively. The value of  $\Delta a_0 = 0.0015$ , used in run ART1 (see Table 1) was determined in a convergence study using a set of  $64^3$  particle simulations described in Kravtsov et al. (1998). To study the effects of time step, we have also run a simulation with  $\Delta a_0 = 0.003$ .

The ART code integrates the equations of motion in *comoving* coordinates. Therefore, if a fixed grid is used to calculate the forces, the force resolution of the simulation degrades as  $\propto a = (1+z)^{-1}$  (see § 1). In order to prevent this and to preserve the initial resolution in *physical* coordinates in the simulations presented in this paper, the dynamic range between the start ( $z_i = 87$ ) and the end ( $z = 0$ ) of the simulation should increase by  $(1+z_i)$ : i.e., for our simulations reach  $128 \times (1+z_i) = 11,136$ .

In the simulations presented in this paper, the peak resolution is reached by creating a refinement hierarchy of five levels of refinement in addition to the base  $128^3$  uniform

**Table 1.** Parameters of the numerical simulations. The corresponding force resolution in  $h^{-1}\text{kpc}$  is included in parenthesis. Note that PM1 and PM2 were simulated using the AP<sup>3</sup>M code, while PM3 and PM4 have been simulated using the ART code with mesh refinement switched off. The number of time steps for the ART simulations is given for the zeroth level; the effective number of time steps for particles on level  $L$  is  $\times 2^L$ , giving 21120 steps for the maximum refinement level of the ART1 run.

simulation	softening	dyn. range	steps
AP <sup>3</sup> M5	0.06 (7.0)	2133	8000
AP <sup>3</sup> M1	0.03 (3.5)	4267	8000
AP <sup>3</sup> M4	0.03 (3.5)	4267	2000
AP <sup>3</sup> M2	0.02 (2.3)	6400	6000
AP <sup>3</sup> M3	0.015 (1.8)	8544	6000
ART1	0.03125 (3.7)	4096	660
ART2	0.03125 (3.7)	4096	330
PM1	3.5 (409)	128	6000
PM2	3.5 (409)	128	1500
PM3	2 (234)	128	1500
PM4	2 (234)	128	750

grid. However, the small number of particles in these simulations does not allow the code to reach the required target dynamic range of 11,136, estimated above.

## 2.3 Simulations

Although we are not directly interested here in cosmological applications we decided to use a definite cosmological model: the cluster normalized,  $\sigma_8 = 0.67$ , standard cold dark matter (SCDM) model. All simulations were run on a  $128^3$  mesh with  $64^3$  particles and started with the same random realization at  $z = 87$ . The adopted box size is  $15h^{-1}$  Mpc, which gives a mass resolution of  $3.55 \times 10^9 h^{-1} M_\odot$ . The AP<sup>3</sup>M simulations were carried out varying both force resolution and time steps. The two runs of the ART code differ only in the number of integration steps on the lowest-resolution of the uniform grid.

For comparison we also ran the PM simulations. Both the AP<sup>3</sup>M and ART have an internal PM block and we ran two pairs of PM simulations using these different PM implementations. This is done to compare implementations and to explore the effects of the time integration scheme on the results. In the case of AP<sup>3</sup>M (PM1 and PM2) both the adaptive and the PP part of the P<sup>3</sup>M code have been switched off, while in the ART PM runs (PM3 and PM4) we have simply switched off mesh refinement. The parameters of the simulations are summarized in Table 1. The force softening is given in grid units and in  $h^{-1}\text{kpc}$  (in brackets), and

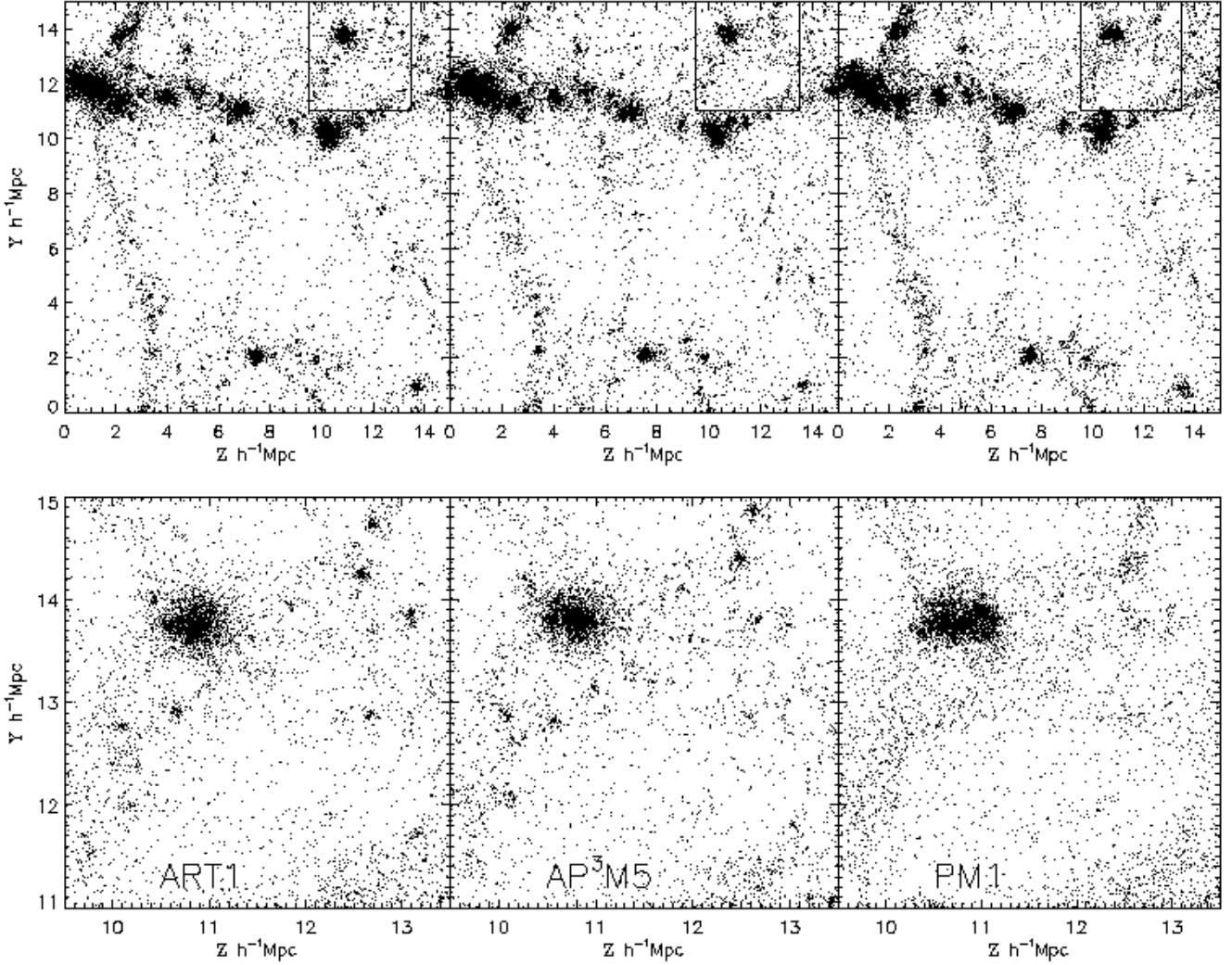


**Figure 1.** Slice of  $3 h^{-1} \text{ Mpc}$  (top row) through the ART (left),  $\text{AP}^3\text{M}$  (middle), and PM(right) simulation. In the bottom row we zoom into the region marked in the top row.

the number of steps of the ART simulations is presented for the lowest-resolution (the effective number on the highest-resolution is 32 times larger).

Using this set of runs we can compare simulations with the same force resolution but different integration steps (e.g.,  $\text{AP}^3\text{M1}$  with  $\text{AP}^3\text{M4}$ , ART1 and ART2) amongst each other and simulations with the same number of integration steps but with varying force resolution (e.g.,  $\text{AP}^3\text{M1}$  with  $\text{AP}^3\text{M5}$ ). Additionally we compare the different  $N$ -body codes in order to quantify the deviations due to different (grid-based) methods to solve the equations of motion.

It is important to keep in mind that the shape of the small-scale force is somewhat different in the codes used. Therefore, equal dynamic range does not correspond to the same physical resolution. The peak resolution of the ART code is  $\approx 2$  cells of the highest level refinement, and so the actual force resolution is twice worse than the “formal” resolution given by the dynamic range. To make cross-code comparison, we have performed the simulation  $\text{AP}^3\text{M5}$ , which has approximately half the dynamic range of the ART runs and similar force resolution.

### 3 PROPERTIES OF THE PARTICLE DISTRIBUTION

#### 3.1 Visual comparison

A first inspection of the global distribution of particles in a  $3 h^{-1} \text{ Mpc}$  thick slice (Fig. 1, top row) shows that the distributions are very similar. Even the much lower resolution PM1 simulation shows virtually the same global particle distribution. In the bottom row of the figure we zoom into the region marked by rectangles in the upper panel. Here one can clearly see that the two high resolution runs produce many small-size dense halos, which are, however, slightly shifted in their positions. We attribute this shift to the cumulative phase errors due to the differences in the time integration schemes of the type observed and discussed in a recent code comparison by Frenk et al. (1999; Santa-Barbara cluster comparison project). Most of these small clumps are absent in the PM run due to its poor resolution. The small scale density peaks do not collapse on scales smaller than the 2 PM grid cells due to the sub-newtonian of self-gravitation at these scales (see § 3.3). From Figure 1 it can be seen that

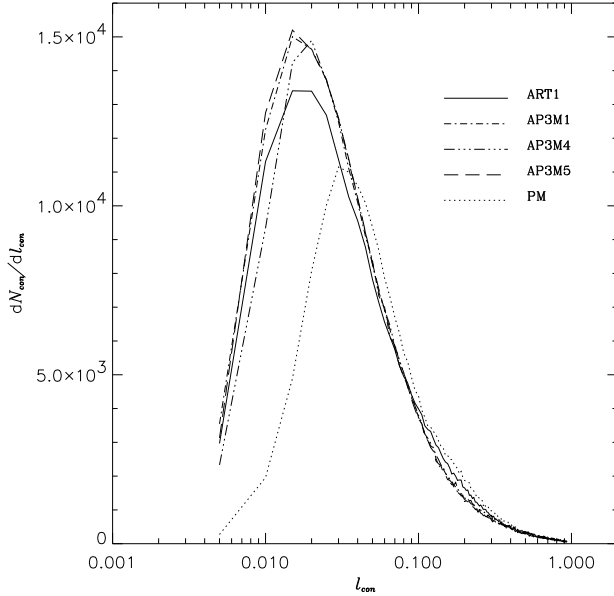


**Figure 2.** Number of connections of the minimum spanning tree per bin of the connection lengths  $l_{con}$  as a function of the connection length. The connection length is in units of the mean interparticle distance  $\bar{l}$ , the bin size is  $dl_{con} = 0.005 * \bar{l}$ .

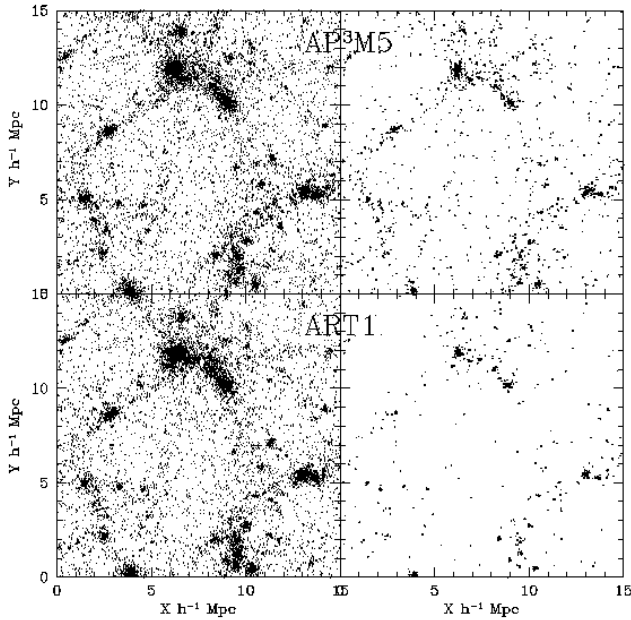


**Figure 3.** Left: Projections of 5% of all particles of the box along the z-axis. Right: Projections of all doublets and triplets found with  $l = 0.015$ . Note that the systems linked using this linking length have overdensity of  $\delta \gtrsim 420000$ .

only halos of size larger than approximately one grid cell collapse in the PM simulation (see, e.g., Klypin 1996).

Our comparison can be contrasted with comparison by Suisalu & Saar (1996) (Fig.1 and Fig.2 in their paper). If compared on a large scale, the particle distributions in different runs compare much better in our case than the sim-

ulations compared in Suisalu & Saar (1996). This indicates that the differences they observed are due to the differences in their multigrid algorithm rather than to the two-body scattering, as argued in their paper.

### 3.2 The minimal spanning tree

To quantify the differences between the simulations we have calculated the minimal spanning tree (MST) of the particle distribution. The minimal spanning tree of any point distribution is a *unique*, well defined quantity which describes the clustering properties of the point process completely (e.g., Bhavsar & Splinter 1996, and references therein). The minimal spanning tree of  $n$  points contains  $N - 1$  connections. For the ART1, AP<sup>3</sup>M1, AP<sup>3</sup>M4, AP<sup>3</sup>M5 and a PM simulations we show in Fig. 2 the number of connections  $N_{con}$  of the tree per bin of the connection length (equal to  $0.005 * \bar{l}$ ) as a function of the length of the connection,  $l_{con}$ . Here,  $\bar{l} = (V_{box}/N)^{1/3}$  denotes the mean inter-particle separation. Since the length of the connection is proportional to  $\rho^{-1/3}$  the probability distribution of connections ( $N_{con}/N$ ) is equivalent to the density probability distribution in the simulation.

In Fig. 2, the connection length distributions for ART and AP<sup>3</sup>M simulations are peaked at the same relative connection length ( $\approx 0.015 - 0.02\bar{l}$ ), whereas the PM simulation is peaked at a higher value ( $\approx 0.03 - 0.04\bar{l}$ ). This indicates the ability of the ART and the AP<sup>3</sup>M codes to resolve shorter scales and, therefore, to reach higher overdensities. The position of the maximum depends only slightly on the resolution. In fact, increasing the resolution from PM to ART by a factor of 32 shifts the maximum by about a factor of 2. This is probably because the differences affect only a very small fraction of the volume and dark matter particles. Correspondingly, differences in resolutions of AP<sup>3</sup>M1 and AP<sup>3</sup>M5 are too subtle to have a visible effect on the distribution.

A time integration has a much more noticeable effect. An increase of the integration step in the run AP<sup>3</sup>M4 compared to AP<sup>3</sup>M1 and AP<sup>3</sup>M5 leads to a shift of the maximum (and distribution) to higher values of  $l_{con}$ . This is caused by inaccuracies in the integration of particle trajectories in high-density regions, as is evidenced, for example, by the halo density profiles in the AP<sup>3</sup>M4 run (see also results below).

The maxima of the AP<sup>3</sup>M simulations are slightly higher in amplitude than the maximum of the ART simulation. This reflects the fact that the AP<sup>3</sup>M resolves forces uniformly (i.e., equally well in both low- and high-density regions). The ART code by design reaches high resolution only in the high-density regions. Therefore, there are groups of a few particles located in low-density environments and thus not resolved by the ART code, which are however resolved by the AP<sup>3</sup>M. For example, we have found 3618 doublets and 558 triplets linked by  $l = 0.015$  (the maximum of the distribution) in the AP<sup>3</sup>M5 run, whereas only 2753 doublets and 466 triplets are found in the ART1 simulation at this linking lengths.

Figure 3 demonstrates that many of the missing doublets and triplets are indeed located in the low-density regions. The right column of this figure shows the projection of the distribution of all doublets and triplets found in the

**Table 2.** Density cross-correlation coefficient  $K = \frac{\langle \delta_1 \delta_2 \rangle}{\sigma_1 \sigma_2}$ .

			grid				
simulation			32	64	128	256	400
ART1	↔	ART2	0.98	0.98	0.94	0.84	0.72
AP <sup>3</sup> M1	↔	AP <sup>3</sup> M4	0.98	0.98	0.98	0.93	0.87
PM1	↔	PM2	1.00	1.00	1.00	1.00	1.00
PM3	↔	PM4	1.00	1.00	1.00	1.00	1.00
AP <sup>3</sup> M2	↔	AP <sup>3</sup> M3	0.98	0.98	0.98	0.93	0.87
AP <sup>3</sup> M1	↔	AP <sup>3</sup> M5	0.98	0.99	0.99	0.96	0.91
PM2	↔	PM3	1.00	0.98	0.93	0.84	0.73
ART1	↔	AP <sup>3</sup> M1	0.95	0.88	0.71	0.44	0.30
ART1	↔	AP <sup>3</sup> M5	0.95	0.88	0.71	0.44	0.30
ART1	↔	PM1	0.96	0.92	0.80	0.60	0.47
AP <sup>3</sup> M1	↔	PM1	0.95	0.90	0.79	0.61	0.48

AP<sup>3</sup>M5 (top) and ART1 (bottom) runs by the friends-of-friends algorithm with the linking length of  $l = 0.015$ . For comparison, we show in the left column of Fig. 3 a projections of randomly selected 5% of all particles. While some doublets in the low-density regions are found in the ART run, all of them are gravitationally unbound (are chance superpositions). We find that in the AP<sup>3</sup>M runs most of such doublets and triplets are bound and are a part of a binary, triple, or higher multiplicity clusters.

According to the sampling theorem, one needs at least  $\sim 20 - 30$  particles to resolve three-dimensional waves in the initial power spectrum. The presence of gravitationally bound clusters consisting of just a few particles is therefore artificial.

### 3.3 Density Cross-Correlation Coefficient

The density cross-correlation coefficient,

$$K = \frac{\langle \delta_1 \delta_2 \rangle}{\sigma_1 \sigma_2}, \quad (2)$$

was introduced by Coles et al. (1993) in order to quantify similarities and differences between simulations of different cosmological models. Recently, Splinter et al. (1998) have adopted this statistic to compare simulations. Here, we follow the same approach and use this measure to quantify differences between simulations which have been carried out by different numerical algorithms or by the same algorithm but with different parameters of the simulation.

To compute  $K$ , we have calculated the densities on a regular mesh using the triangular-shaped cloud (TSC; Hockney & Eastwood 1981) density assignment scheme and then

used the resulting density field to compute  $\langle \delta_1 \delta_2 \rangle$  and variances. We have varied the size of the grid in order to show the dependence of the cross-correlation on the smoothing scale of the density field.

We summarize our results in Table 2: the first four rows present the cross-correlation coefficients between the runs with the same time integration scheme but different time steps. In the following two rows we present the cross-correlation coefficients for the AP<sup>3</sup>M runs with different force resolutions but the same integration step. The rest of the rows in the table present the cross-correlation coefficients for the runs with different time integration schemes as well as the cross-correlation coefficients between the AP<sup>3</sup>M1 and PM1 runs which have been simulated with the same time integration scheme but with vastly different force resolutions.

In all cases, it is obvious that the cross-correlation worsens for smaller smoothing scales (the larger density grid size). With smaller smoothing, smaller structures in the density field are resolved. The degraded cross-correlation therefore indicates that there are differences in locations and/or densities of these small-scale structures. It is also clear from the definition of  $K$  that this measure is particularly sensitive to the differences in the highest density regions. If we restrict the correlation analysis to a coarse grid, we smooth the particle distribution with a fairly large smoothing length and smear out the details and differences of the small-scale structure.

The differences revealed by the cross-correlation coefficient can arise either because the internal density distribution of the structures is different in different runs or because the spatial locations of these structures are somewhat different. Our analysis of halo profiles (See § 4.5) shows that differences in density in the same halos are small (except, of course for the PM runs) and have no significant effect on the cross-correlation. The degrading cross-correlation in high-resolution runs is thus due to the differences in the locations of small-scale structure rather than to the differences in density. Indeed, one can readily see in the bottom row of Fig. 1 that positions of small clumps in the ART and AP<sup>3</sup>M simulations often differ by  $\sim 100 - 300h^{-1}$  kpc, the scale at which a significant decrease in  $K$  is observed. With such shifts in halo locations, the same halo may occupy different cells in the density grid which systematically reduces  $\langle \delta_1 \delta_2 \rangle$  (calculated cell-by-cell) and results in a lower  $K$ .

What causes the differences in halo positions? The rows 1, 2, 5, and 6 of Table 2 indicate that both force resolution and time step have the same effect on  $K$ , both causing some phase errors. However, rows 7-9 show that the time integration scheme causes much bigger phase differences than either force resolution or time step. This was indeed observed in the recent ‘‘Santa Barbara Cluster’’ code comparison project (Frenk et al. 1999). Different time integration schemes lead to a different accumulation of the phase errors. The manifestation of these differences is certain ‘‘asynchronicity’’ between simulations: the same phase error is accumulated at slightly different time moments. This results in shifts of halo positions when simulations are compared at the same time moment.

We have indeed observed such asynchronicity in our simulations. Thus, for example, cross-correlation coefficient  $K$  between ART1 and AP<sup>3</sup>M5 on a 128<sup>3</sup> grid reaches a maximum of 0.84 at  $a = 1.04$  when AP<sup>3</sup>M5 is evolved further in

time (this can be compared to 0.71 at  $a = 1.0$  in Table 2) while keeping ART1 fixed at  $a=1.0$ . Similar effect is observed at  $z = 2$ : the maximum  $K$  is achieved when AP<sup>3</sup>M5 is advanced forward in time by a factor of 1.02 in expansion factor. Partly, this asynchronicity may be caused by the initial phase error introduced at the start as the AP<sup>3</sup>M simulations particles were advanced half a step (or by a factor of 1.03 in expansion factor) forward. The additional error accumulates during the time integration.

While most halo properties and properties of the matter distribution appear to be similar in the ART and the AP<sup>3</sup>M runs (see results below), the differences between positions of small-scale structures are much larger between these runs than any differences between runs simulated using the same code. This is clearly seen in the case of PM runs. All 4 runs cross-correlate perfectly within the code type (PM1 and PM2 were run using AP<sup>3</sup>M, while PM3 and PM4 were run using the ART code), but cross-correlate rather poorly when different code simulations are compared. In the latter case we observed a decrease of  $K$  as we go to smaller smoothing scales similar to that observed in other cross-code cross-correlation coefficients.

One should of course bear in mind that the shape and accuracy of the PM force in AP<sup>3</sup>M and ART codes are somewhat different at small ( $\sim 1 - 4$  grid cells) scales. In the AP<sup>3</sup>M, the PM force is shaped using modification of the Green functions (Couchman 1991) which is controlled by a special softening parameter  $\epsilon_{\text{PM}}$ . This procedure considerably increases accuracy of the force (down to  $\lesssim 5\%$  in the case of  $\epsilon_{\text{PM}} \approx 3.5$  used in our PM1 and PM2 simulations) in the force, at the expense of making the force somewhat “softer”. Thus, for example, in PM1 and PM2 runs, the force becomes systematically smaller than the Newtonian value at separations  $\lesssim 3$  grid cells (15% smaller at  $r = 2$  cells and 70% smaller at  $r = 1$  cell). The Green functions in the PM solver in the ART code are not modified to reduce the errors. This results in the force which is Newtonian on average down to the scale of one grid cell (the force then falls off sharply at smaller separations). At the same time, the errors at small separations are considerably higher (see Gelb 1992; Kravtsov et al. 1997). At separation of 1 grid cell, the errors may reach  $\sim 50\%$  (albeit in small number of particle configurations). About 10 – 20% of that error is due to the cubical shape of the particles assumed in the PM algorithm, while the remaining error arises from numerical differentiation of the potential. These errors, however, are not systematically positive or negative but are scattered more or less evenly around zero. This means that particle trajectories can be integrated stably down to separations of 1-2 grid cells, as was demonstrated in Kravtsov et al. (1997).

Although it is important to keep the differences in force shape and accuracy in mind, we think that they are not the main cause of poor cross-correlations. The halo density profiles in different PM runs are in good agreement at all resolved scales and thus differences in internal density distributions cannot explain low cross-code  $K$ . At the same time, visual comparisons of halo positions show small shifts that are most naturally explained by the different phase errors accumulated in different codes.

This calls into question the usefulness of cross-correlation coefficient for studies of resolution effects (Splinter et al. 1998), unless the study is done within the same numerical code.

ter et al. 1998), unless the study is done within the same numerical code.

This conclusion can, in fact, be drawn from results of Splinter et al. (1998): when the simulation evolves into the highly nonlinear stage the cross-correlation within the same code is much better than cross-correlation between runs of similar resolution but simulated using different codes. For example their Table 4 shows that on a  $128^3$  grid coefficient  $K$  for the TREE-code runs with the force resolutions of  $\epsilon = 0.0625$  and  $\epsilon = 0.25$  (in the units of mean interparticle separation) is 0.87, while the cross-correlation coefficient between the TREE  $\epsilon = 0.0625$  and AP<sup>3</sup>M  $\epsilon = 0.25$  runs is only 0.67. This is similar to the value of 0.71 which we obtained for  $K$  on the same grid size for ART1 and AP<sup>3</sup>M runs. Moreover, Figure 9 in Splinter et al. (1998) also agrees with our conclusion. The phase errors demonstrated in this figure increase towards smaller scales which explains the decrease of cross-correlation coefficient for finer grids. Moreover, the figure also shows that cross-correlation *within single code type* is always good regardless of the mass or force resolution. The largest phase differences are observed between runs simulated using different codes.

The differences in time integration schemes are not the only possible sources of small-scale differences in density fields. For example, the last two rows of Table 2 show that cross-correlation between high-resolution ART and AP<sup>3</sup>M runs and low-resolution PM run is poor regardless of whether the integration scheme was the same (AP<sup>3</sup>M1  $\leftrightarrow$  PM1) or different (ART1  $\leftrightarrow$  PM1). In this case, the differences in the small-scale details of density fields are due to the vastly different force resolutions of the simulations. As was noted above, the low resolution of the PM simulation ( $234h^{-1}$  kpc) precludes collapse of any halos with the size smaller than  $\sim 1 - 2$  grid cells (see Fig. 1). In the locations of small-size halos  $\delta$  is very high for ART and AP<sup>3</sup>M runs but is much lower (because there are no halos) in the PM run; hence the considerably lower cross-correlation coefficient.

Given the above considerations, our interpretation of our results and the results of Splinter et al. (1998) is markedly different than the interpretation by the authors of the latter study. These authors interpret the differences between the low- and high-resolution runs as an erroneous evolution in the latter, whereas our interpretation (obvious from Fig. 1) is that these differences are due to the fact that high-density small-scale structures such as halos do not collapse in low-resolution runs. The differences between high-resolution runs are interpreted as the phase errors leading to small shifts to the locations of small-scale structures, as discussed above and as observed in other studies (Frenk et al. 1999).

The origin of these phase errors is the dynamical instability of particle trajectories in the high-density regions. As is well known, the trajectories in the virialized systems tend to be chaotic and any small differences existing at any time moment will tend to grow very fast with time. The divergence can thus be expected to be more important in nonlinear regions and this explains the larger phase errors at smaller scales. The differences may be caused by the difference in the force calculation, errors introduced by numerical time integration, or simply by different roundoff errors. The resulting phase errors are cumulative and thus will grow with time.



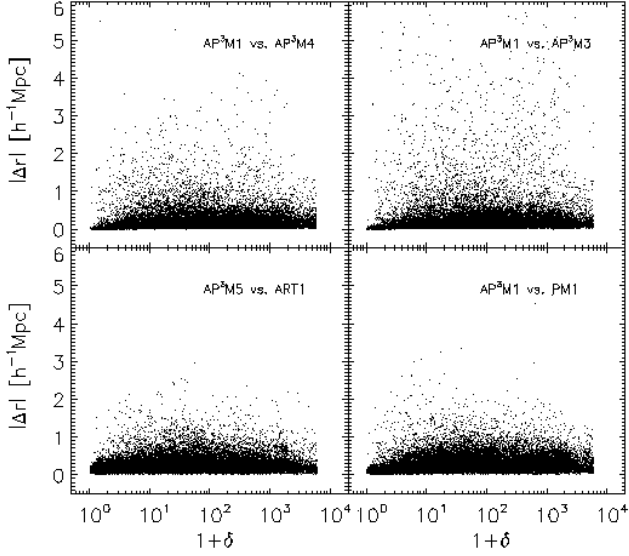


**Figure 4.** Deviation of particle coordinates at  $z = 0$  in two simulations (started with identical initial particle distribution) depending on the local overdensity (estimated using  $128^3$ -cell grid) at the location of particle in the first simulation. Only 10% of all particles are shown. In the upper panel of Fig. 4 we compare runs simulated using the same code but different integration steps (left) and different force resolution (right). In the lower panel we compare runs simulated using different codes.

Unfortunately, it is impossible to tell which code has the smallest phase errors, because we do not know how the phases should evolve in the high-density regions. However, this is probably not the point. Phase errors of this kind will be very difficult to get rid of, because even in the case of infinitely good mass, force, and time resolutions, there will always be roundoff errors, which will behave differently in different codes and thus will tend to grow differences in phases. Luckily, almost all popular statistics used in cosmological analyses are not sensitive to phases and therefore results are not affected by this problem. Moreover, it is clear that at scales  $\gtrsim 1h^{-1}$  Mpc the errors in phases become negligible (different runs cross-correlate perfectly) and therefore even phase-sensitive analyses should not be affected if restricted to large scales. However, it is clear that the existence of such errors should be kept in mind when analyzing or comparing cosmological simulations.

### 3.4 Particle trajectories

As we have discussed in the previous section, small numerical errors tend to grow and lead to deviations of the particle trajectories in nonlinear regions. Nevertheless, it is clear that the maximum deviations should be approximately equal to the size of a typical halo. Although particle trajectories can deviate, they are expected to stay bound to the parent halo. There is an additional deviation of the order of  $\sim 100 - 300h^{-1}$  kpc in the positions of the halos themselves (due to the phase errors), but this is also of the order of halo size. All in all, we can expect a scatter in the positions of the same particles in different simulations not larger than the size of the largest systems formed:  $\sim 1 - 2h^{-1}$  Mpc.

To compare the particle trajectories in our simula-

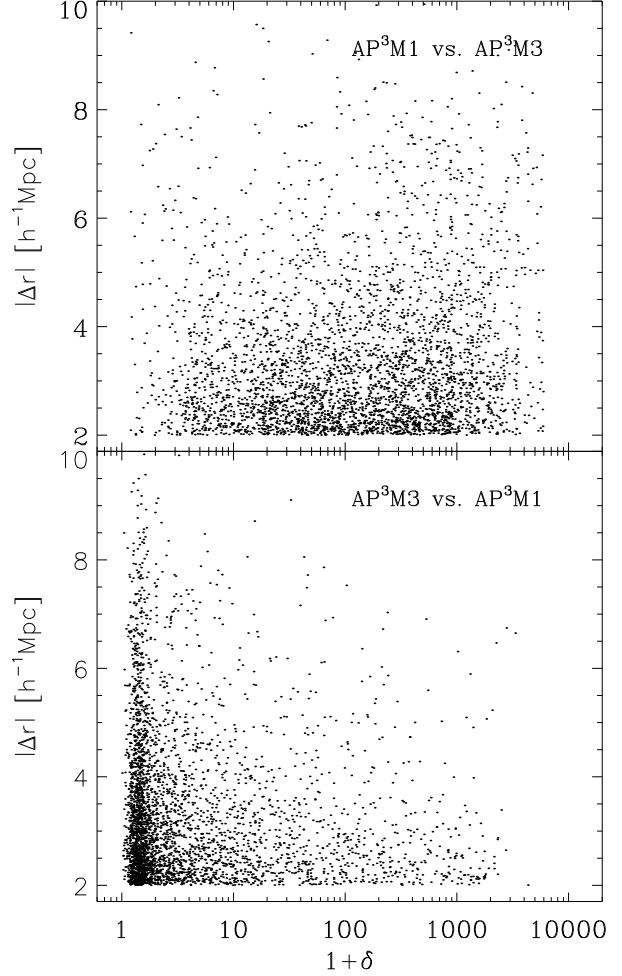


**Figure 5.** The same as in Fig. 4 but for the runs AP³M1 and AP³M3. In this case *all* particles with  $|\Delta r| > 2h^{-1}$  Mpc are shown (these particles constitute  $\approx 1.4\%$  of the total number of particles). The overdensity in the upper panel is estimated at the location of the particle in the AP³M1 run, while in the bottom panel it is estimated for the corresponding particle in the AP³M3 run. Note that counterpart particles in AP³M3 tend to be located in low-density regions.

tions, we have calculated the deviations of the coordinates  $\Delta r = |\vec{r}^{(1)(k)} - \vec{r}^{(2)(k)}|$ , where  $\vec{r}^{(i)(k)}$  is the position of the  $k$ -th particle in the  $i$ -th simulation.

In Fig. 4 we have plotted  $\Delta r$  as a function of the local overdensity at the position of the particle  $\vec{r}^{(1)}$  for 10% of particles randomly selected from the total number of particles. In the upper panel of Fig. 4 we compare runs simulated using the same code but different integration steps (left) and different force resolution (right). In the lower panels we compare runs simulated using different codes.

A quick look at Fig. 4 shows that the scatter in particle positions is substantial but in most runs it is contained within  $\lesssim 2h^{-1}$  Mpc, the approximate size of the largest system seen in Fig. 1. The scatter for *most* particles in cross-code differences shown in the bottom row is somewhat larger due to the larger differences in halo positions. As mentioned above, this difference adds to the difference in particle posi-

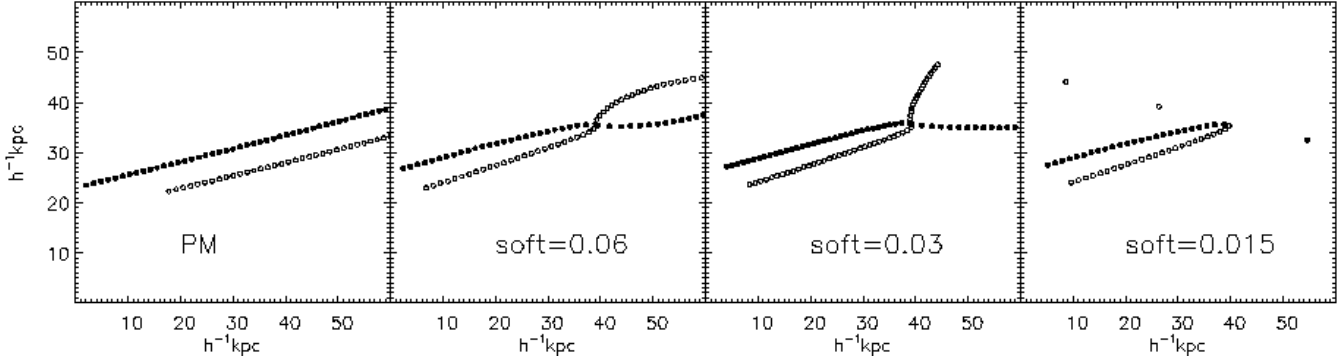


**Figure 6.** Trajectory of two particles in AP<sup>3</sup>M simulation for different force resolutions ( $\Delta t = \text{const}$ ). The figure demonstrates the presence of two-body scattering in all of our AP<sup>3</sup>M simulations.

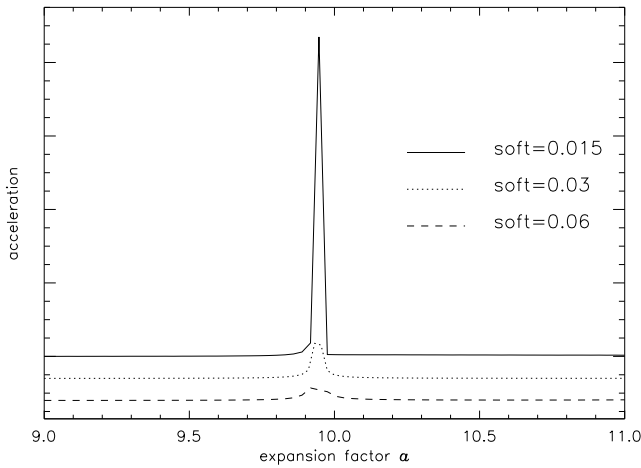


**Figure 7.** Acceleration (in arbitrary units) of particle denoted with filled circles in Fig. 6. Dotted and dashed curves lowered by a constant offset.

tions *within* halos. However, the scatter is even larger when AP<sup>3</sup>M1 and AP<sup>3</sup>M3 are compared. In this case, about 1.4% of particles are separated by more than  $2h^{-1}$  Mpc. We did not find such outliers when comparing ART runs or AP<sup>3</sup>M runs with lower resolution amongst themselves. The comparison of AP<sup>3</sup>M5 and ART1 shows that the scatter is much smaller.

Figure 5 shows *all* the particles with separations  $|\Delta r| > 2h^{-1}$  Mpc in the AP<sup>3</sup>M1 and AP<sup>3</sup>M3 runs. The overdensity in the upper panel is estimated at the location of the particle in the AP<sup>3</sup>M1 run, while in the bottom panel it is estimated for the corresponding particle in the AP<sup>3</sup>M3 run. It is clear that counterpart particles in the AP<sup>3</sup>M3 tend to be located in low-density regions, whereas the corresponding particles in the AP<sup>3</sup>M1 run are located in a wide range of environments.

The fact that these large deviations occur preferentially in the highest resolution runs, immediately raises suspicion that they are due to two-body scattering. Indeed, when we analyzed the trajectories of the deviant pairs, we found obvious scattering events. In Fig. 6 we present an example of such two-body scattering. In this figure the force resolution

increases (softening decreases) from right to left. For clarity only every second integration step is shown.

The region shown in Fig. 6 is smaller than the grid cell size, so there is no interaction at all in the PM simulation. The two particles move in the mean potential of the other particles. The same happens in the ART simulations. On the contrary, due to the high force resolution these two particles interact and approach in the case of AP<sup>3</sup>M 1-4 runs. In the case of the highest force resolution this leads to an interaction which, due to the insufficiently small time step, leads to a violation of energy conservation. The particles approach very closely, feel a large force, undergo in this moment a huge acceleration and move away in opposite directions with high velocities. At the next integration step the particles are already too far to feel substantial two-body interaction. Therefore, they move with almost constant high velocity in opposite directions. The velocity is about a factor of 10 higher than the initial velocity, i.e. the total kinetic energy of the system increased during the interaction by a factor of 100. Such pairs of particles are located at large  $\Delta r$  in scatter plots shown in Figs. 4 & 5. We have run an additional simulation with the parameters identical to those of the AP<sup>3</sup>M3 run but with a much larger number of time steps (48,000 steps in total). The outlying particles disappear and the plots look similar to the AP<sup>3</sup>M5-ART1 plot. This means that although the scattering is still present, there is no violation of energy conservation in the smaller step run and therefore there are no high-velocity streaming particles.

Fig 5 indicates that scattered particles attain large velocities and move out of high-density regions. Most of the simulation volume is low-density, so it is not surprising that we find these streaming particles preferentially in the low-density regions. Their counterparts in the AP<sup>3</sup>M1 runs, on the other hand, are located in a wide range of environments. This implies either that the scattered particles were ejected from high-density regions, or that these particles attained their excess energy in two-body encounters in low-density regions and simply did not participate in the gravitational collapse due to their high velocities.

Fig. 7 shows the acceleration of the particle denoted by filled circles in the three AP<sup>3</sup>M plots in Fig. 6. This figure illustrates the spike in the particle acceleration during the scattering event. It also shows that the higher the force resolution, the larger the acceleration.

Such collisions are possible if the force resolution is in-

dependent of the local particle density. This problem does not arise in the ART code because the resolution is only increased in the regions of high local particle density. We have checked all particles beyond separation  $\Delta r \gtrsim 2h^{-1}\text{Mpc}$  within the both ART runs and could not find any event comparable to the collision in the AP<sup>3</sup>M runs.

The conditions for two-body scattering can be estimated by noting that strong scattering occurs when the potential energy of two-body interaction is equal to kinetic energy of the interacting particles. This gives the scale  $s = 2Gm/v^2$  or

$$s = 8.61 \times 10^{-2} h^{-1} \text{ kpc} \left( \frac{m_p}{10^8 h^{-1} \text{ M}_\odot} \right) \left( \frac{v}{100 \text{ km/s}} \right)^{-2}. \quad (3)$$

For the simulations presented here ( $m_p = 3.55 \times 10^9 h^{-1} \text{ M}_\odot$ ) this scale is

$$s = 3.05 \times v_{100}^{-2} h^{-1} \text{ kpc}, \quad (4)$$

where  $v_{100}$  is velocity in units of 100 km/s. In terms of the mean interparticle separation,  $d = \bar{n}^{-1/3}$ , this gives

$$\tilde{s} \equiv s/d = 0.013 \times v_{100}^{-2}. \quad (5)$$

Two-body scattering occurs if the force resolution,  $\epsilon$ , is less than the scale  $s$  and if  $s$  is much smaller than the *local* interparticle separation  $d_{loc}$ . The latter for these simulations is  $d_{loc} = 234.38(1 + \delta)^{-1/3} h^{-1} \text{ kpc}$ .

The above equations show that scattering is possible in the AP<sup>3</sup>M runs 1 through 4. This in agreement with results presented in Figures 4 and 7.

### 3.5 2-point correlation function

In Fig. 8 we show the correlation function for the dark matter distribution down to the scale of  $5h^{-1} \text{ kpc}$ , which is close to the force resolution of all our high-resolution simulations. The correlation function in runs AP<sup>3</sup>M1 and ART2 are similar to those of AP<sup>3</sup>M5 and ART1 respectively and are not shown for clarity. We can see that the AP<sup>3</sup>M5 and the ART1 runs agree to  $\lesssim 10\%$  over the whole range of scales. The correlation amplitudes of runs AP<sup>3</sup>M 2–4, however, are systematically lower at  $r \lesssim 50 - 60h^{-1} \text{ kpc}$  (i.e., the scale corresponding to  $\approx 15 - 20$  resolutions), with the AP<sup>3</sup>M3 run exhibiting the lowest amplitude. At scales  $\lesssim 30h^{-1} \text{ kpc}$  the deviations from the ART1 and the AP<sup>3</sup>M5 runs are  $\approx 100 - 200\%$ . We attribute these deviations to the numerical effects discussed in § 5. The fact that the AP<sup>3</sup>M2 correlation amplitude deviates less than that of the AP<sup>3</sup>M3 run, indicates that the effect is very sensitive to the force resolution.

The correlation function of the PM simulation deviates strongly on small scales. However, the bend coincides with the force resolution ( $\approx 234h^{-1} \text{ kpc}$ ) of this run. At scales smaller than resolution, we can expect an incorrect correlation amplitude because waves of wavelength smaller than the resolution do not grow at the correct rate in these runs.

This result agrees with the correlation function comparison done by Colín et al. (1999), where agreement of  $\lesssim 10\%$  was found between the correlation functions from the larger 256<sup>3</sup>-particle ART, AP<sup>3</sup>M, and PM simulations at all resolved scales. There is no evidence therefore, that high-resolution simulations, given that they are done with

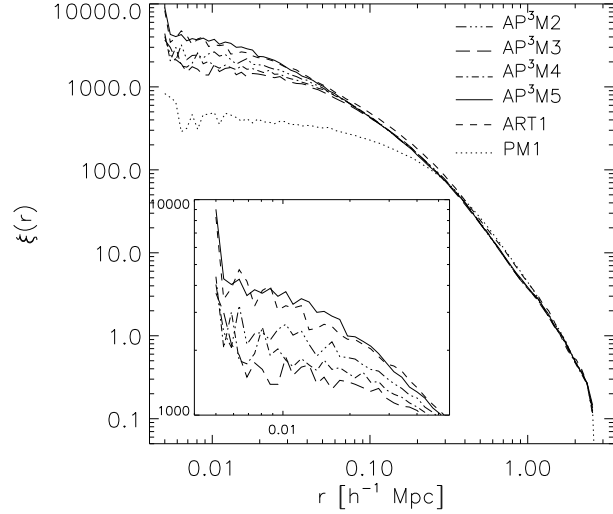


**Figure 8.** Correlation function of dark matter particles. Note that the range of correlation amplitudes is different in the inset panel.

sufficiently small time step, simulate the 2-point correlation function incorrectly at scales smaller than the mean interparticle separation. The agreement between high-resolution and PM simulations of the same mass resolution always agree at the scales resolved in the PM runs.

## 4 PROPERTIES OF HALOS

### 4.1 Identification of Halos

To compare properties of the halos and their distribution in different simulations, we identify DM halos using the friends-of-friends (FOF) algorithm. The algorithm identifies clumps in which all particles have neighbors with distances smaller than  $ll$  times the mean inter particle separation,  $r_{ij} \leq ll \times \bar{r}$ . This halo finding algorithm does not assume a special geometry for the identified objects. A drawback is that it only uses particle positions and therefore can identify spurious unbound clumps at low halo masses.

The mean overdensity of a particle cluster is related to the linking length used to identify it. In an Einstein-de-Sitter universe (simulated in our runs) virialized halos have an overdensity of  $\delta_{vir} \approx 178$ , which corresponds approximately to the linking length of  $ll = 0.2$ . A reduction of the linking length by a factor of 2 roughly corresponds to an increase of the overdensity by a factor of 8. Using smaller linking lengths we can study the substructure of the DM halos. Table 3 lists the number of halos identified using different linking lengths in different runs for the two lower limits on the number of particles in a halo: 25 (columns 2–4) and 50 (columns 5–7).

The table shows that there are differences of  $\sim 15 - 50\%$  between high-resolution runs. The differences are present not only at low linking lengths, but even at the “virial” linking length,  $ll = 0.2$ . These differences are partly due to the nature of the FOF algorithm: small differences in the particle configurations may lead to an identification of a single halo in one simulation and to the identification of two or

**Table 3.** Number of DM halos identified using the FOF algorithm as a function of the linking length (in units of mean interparticle separation). Only halos containing more than 25 (columns 2–4) and 50 (columns 5–7) particles have been counted.

linking length:	$N_p > 25$			$N_p > 50$		
	0.2	0.1	0.05	0.2	0.1	0.05
AP <sup>3</sup> M5	388	292	162	206	152	85
AP <sup>3</sup> M1	377	264	160	204	149	84
AP <sup>3</sup> M4	340	221	110	187	120	65
AP <sup>3</sup> M2	365	251	122	188	132	74
AP <sup>3</sup> M3	332	215	87	173	117	55
PM1	214	150	50	134	74	19
PM2	208	155	49	129	66	18
ART1	359	291	161	199	148	89
ART2	383	297	169	206	156	87

more halos in another simulation. Nevertheless, some systematic differences are also apparent. PM simulations have almost half as many halos due to the absence of small-mass halos (see Fig. 1) that do not collapse (or do not survive) due to the poor force resolution of these runs.

Also, while AP<sup>3</sup>M1, AP<sup>3</sup>M5, ART1, and ART2 runs agree reasonably among themselves, the number of halos in runs AP<sup>3</sup>M2, AP<sup>3</sup>M3, and AP<sup>3</sup>M4 is systematically lower. In this case the differences seem to be counter-intuitive: the number of halos is smaller in higher force resolution runs. These differences persist at all linking lengths indicating that there are differences in substructure as well as in the number of isolated halos. Moreover, the differences persist even for a larger cut in the number of particles. It has been noted in previous studies (e.g., van Kampen 1995; Moore, Katz & Lake 1996) that particle evaporation due to two-body scattering (see, for example, Binney & Tremaine 1987) can be important for halos of  $\lesssim 30$  particles. For such halos the evaporation time-scale, especially in the presence of strong tidal fields, can be comparable to or less than the Hubble time. However, for halos containing  $\gtrsim 50$  particles, evaporation should be negligible. Nevertheless, the trend with resolution seen in Table 3 does suggest that two-body evaporation is the process responsible for the differences.

The most likely explanation of these results is, in our opinion, the accuracy of the time integration. The estimates of the evaporation time-scale are done assuming no errors in energy exchange between particles in a scattering event. Our analysis of such events in our simulations, on the other hand, shows that with the time step of the AP<sup>3</sup>M 2-4 runs, there is severe energy conservation violation during scatterings. The particles attain much larger velocities than they should have if the integration were perfect. For example, in the scattering event shown in Fig. 6 the final kinetic energy

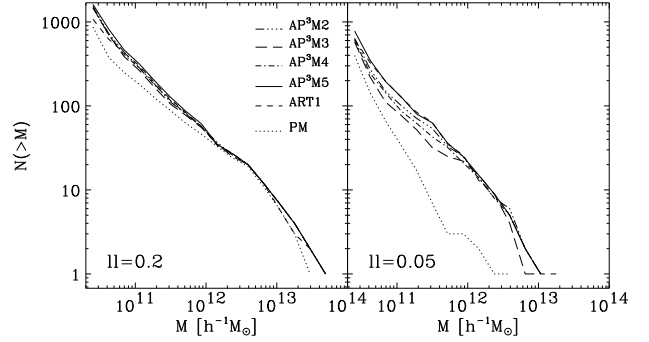


**Figure 9.** Mass function for some simulations and two linking lengths.

of the two particles is 100 times larger than their initial kinetic energy. Therefore, a time step that is insufficiently small to properly handle two-body scattering may exacerbate the process of evaporation and result in much shorter than predicted evaporation time-scales, even for halos containing relatively large numbers of particles. The differences between AP<sup>3</sup>M1 run and runs AP<sup>3</sup>M2 and 4 indicate that this effect is very sensitive to both the force resolution and to the time step of the simulation.

Another possible explanation is that halos do not evaporate but the particles are heated due to non-conservation of energy which makes halos “puffier”. Such halos would be more prone to destruction by tides in high-density regions.

## 4.2 Mass Function

In Fig. 9 we show the mass functions of all halos identified with various linking lengths at  $z = 0$ .

As can be seen in the left panel of Fig. 9, the halo mass function in the PM run is biased towards large masses: the number of objects of mass  $\gtrsim 2 \times 10^{12} h^{-1} M_\odot$  in the PM run agrees well with the corresponding number in the high-resolution runs, while at lower masses the number of halos is strongly underestimated. Mass  $2 \times 10^{12} h^{-1} M_\odot$  corresponds to the virial radius (at  $z = 0$ ,  $\delta_{\text{vir}} = 178$ ) of  $R_{\text{vir}} \approx 213 h^{-1} \text{ kpc}$ , i.e. very close to the force resolution of the PM runs ( $234 h^{-1} \text{ kpc}$ ). The conclusion is that the PM runs fail to reproduce the correct abundances of halos with the virial radius less than about two grid cell sizes.

At smaller linking length,  $ll = 0.05$ , (right panel of Fig. 9) the PM run severely underestimates the halo abundances. We attribute this also to the poor force resolution of the run. The poor resolution prevents the formation of dense cores in the inner regions of collapsed halos and halos that do not reach overdensity of  $\approx 11,000$  (overdensity of objects identified with  $ll = 0.05$ ) will be missed. Even if the central density of some halos reaches this value, the halos are still considerably less dense than their counterparts in the high-resolution runs and are therefore more susceptible to destruction by the tidal fields in high-density regions (Moore et al. 1996; Klypin et al. 1999).

The mass functions of the high-resolution runs agree to  $\sim 30\%$  for isolated halos of overdensity  $\delta = 178$  ( $ll = 0.2$ ). The AP<sup>3</sup>M runs have a larger number of identified halos at masses  $\lesssim 5 \times 10^{10} h^{-1} M_\odot$  (i.e., halos containing  $\lesssim 15$  particles) than the ART runs. This difference is due to smaller number

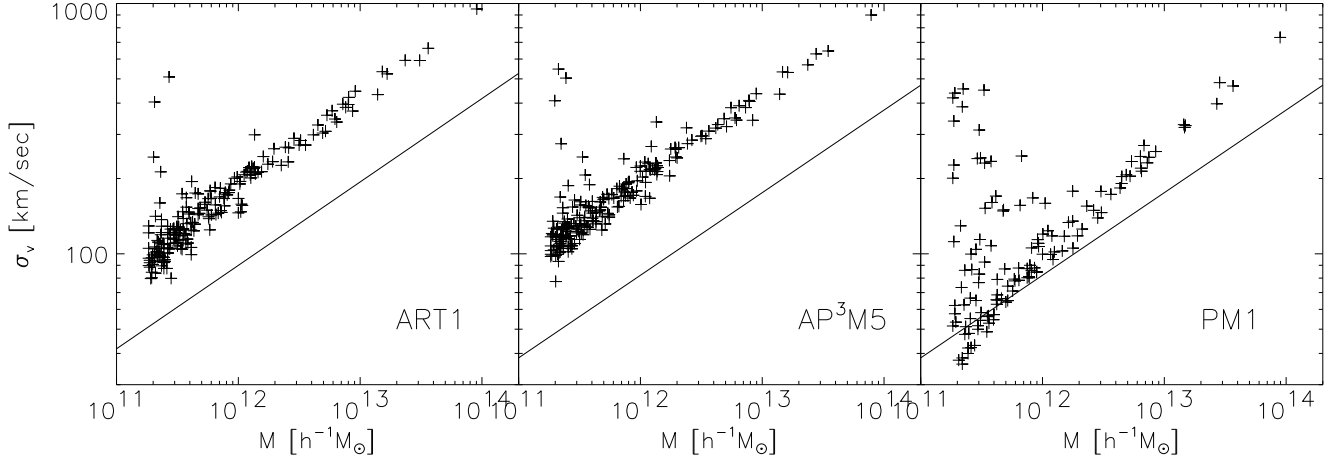


**Figure 10.** Correlation between the velocity dispersion and mass of halos for ART1, AP<sup>3</sup>M1, and PM. Only halos with more than 50 particles are taken into account. The solid line denotes  $\sigma_v \propto M^{1/3}$

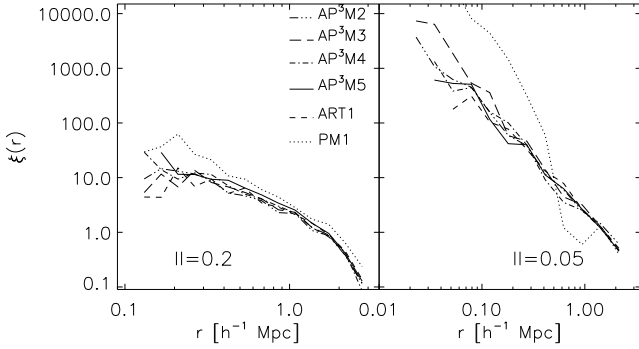


**Figure 11.** Correlation function of halos for some simulations and two linking lengths. A mass cut of 25 particles was used to construct halo catalogs.

of small halos in low-density regions in the ART runs discussed in § 3.2. The mass functions of the AP<sup>3</sup>M1, AP<sup>3</sup>M5, and the ART runs agree well at masses  $\gtrsim 10^{11} h^{-1} M_\odot$  for both  $l = 0.2$  and  $l = 0.05$  (overdensity of 178 and 13000, respectively), indicating that both runs produced similar populations of halos with similar central densities. The mass functions of the AP<sup>3</sup>M 2-4 runs are similar for  $l = 0.2$ , but show differences for  $l = 0.05$ . Thus, for example, the abundance of halos of mass  $\sim 10^{11} - 10^{12} h^{-1} M_\odot$  ( $\sim 30 - 300$  particles) in the AP<sup>3</sup>M3 run is underestimated by a factor of  $\approx 1.5 - 2$ . The mass functions of the AP<sup>3</sup>M2 and AP<sup>3</sup>M4 runs lie in between those of the AP<sup>3</sup>M3 and AP<sup>3</sup>M5 runs.

The fact that differences are present at small linking length indicates differences in the high-density regions. This may be due to the generally lower inner densities of halos and/or to the destruction of “heated” satellites discussed above.

### 4.3 Halo correlation function

Figure 11 shows the 2-point correlation function of identified DM halos. There is good agreement between the correlation functions of isolated virialized ( $l = 0.2$ ) halos in high-resolution runs. Similar to the dark matter correlation

function, the agreement is better than 10%. The agreement between the AP<sup>3</sup>M1, AP<sup>3</sup>M5, and the two ART runs does not break even at higher overdensities ( $l = 0.05$ ), which indicates that these runs produced similar small-scale substructures in the high-density regions within isolated halos. We do not find any differences of the type seen in the DM correlation function (§ 3.5) between AP<sup>3</sup>M runs at  $l = 0.2$ . For halos identified using  $l = 0.05$  some differences are observed, but these are comparable to the poisson errors and are therefore inconclusive.

On the other hand, halos in the PM simulation exhibit higher correlations than halos in the high-resolution runs. As discussed in the previous section, the halo mass function in the PM run is biased toward high masses. The higher amplitude of the correlation function can thus be explained by the mass-dependent bias: higher mass halos are clustered more strongly.

### 4.4 Velocity Dispersion vs. Mass

Figure 10 shows the correlation of velocity dispersion and mass for one of the ART, AP<sup>3</sup>M, and PM simulations. A correlation  $\sigma_v \propto M^{1/3}$  is expected for virialized halos. For the ART1 and AP<sup>3</sup>M5 simulations, the best fit slope of the correlation for the 50 most massive halos is 0.33 (the correlation for the rest of the AP<sup>3</sup>M runs is similar). The velocity dispersion of low-mass halos scatters around this value. For comparison, a line of slope 1/3 is included in all three panels. It should be mentioned here that at the low mass end the FOF groups contains only a few particles so that  $\sigma_v$  is not well determined because the error due to unbound particles accidentally linked by the FOF algorithm may be very high.

The halos in the PM run deviate from the expected slope at masses  $\lesssim 10^{13} h^{-1} M_\odot$ . The virial radii of the halos of these masses are  $\lesssim 364 h^{-1} \text{ kpc}$ . Their size is thus  $\lesssim 3$  force resolutions across. Therefore, the potential and the internal dynamics of the particles in these halos are underestimated by the PM code leading to a steeper slope of the  $\sigma_v - M$  relation.

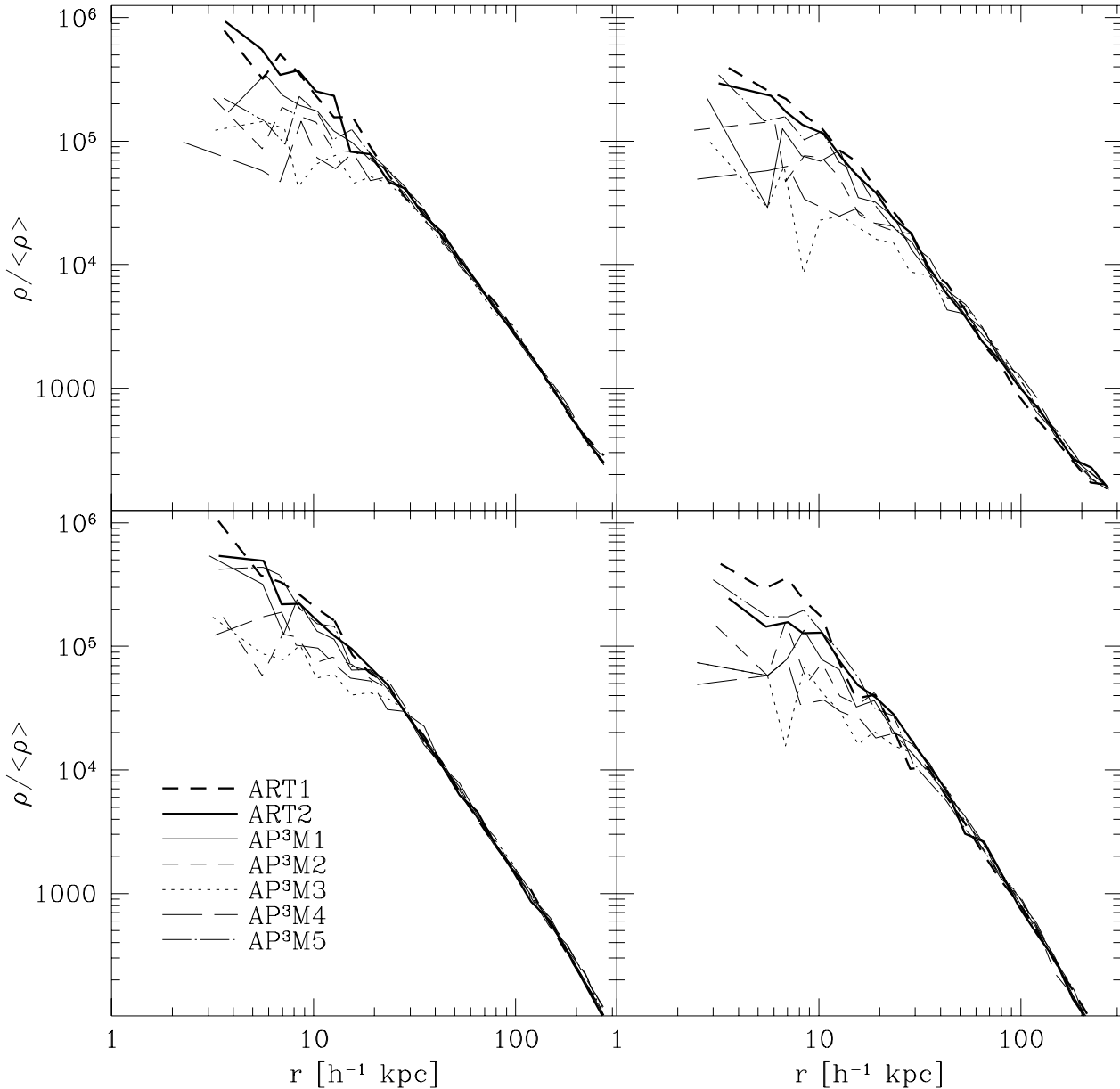


**Figure 12.** Density profiles of halos in different runs.

#### 4.5 Density Profiles

In this and the next two sections we present halo-to-halo comparison of individual halos in different simulations. In this section we will compare the density profiles of DM halos. The density distribution of hierarchically formed halos is currently a subject of debate (see, e.g., Navarro, Frenk & White 1997; Kravtsov et al. 1998; Moore et al. 1999) and study of the resolution effects and cross-code comparisons are therefore very important. In figure 12 we present the density profiles of four of the most massive halos in our simulations. We have not shown the profile of the most massive halo because it appears to have undergone a recent major

merger and is not very relaxed. In this figure, we present only profiles of halos in the high-resolution runs. Not surprisingly, the inner density of the PM halos is much smaller than in the high-resolution runs and their profiles deviate strongly from the profiles of high-resolution halos at the scales shown in Fig. 12. We do not show the PM profiles for clarity.

A glance at Fig. 12 shows that all profiles agree well at  $r \gtrsim 30 h^{-1}$  kpc. This scale is about eight times smaller than the mean interparticle separation. Thus, despite the very different resolutions, time steps, and numerical techniques used for the simulations, the convergence is observed at a scale much lower than the mean interparticle separation, ar-

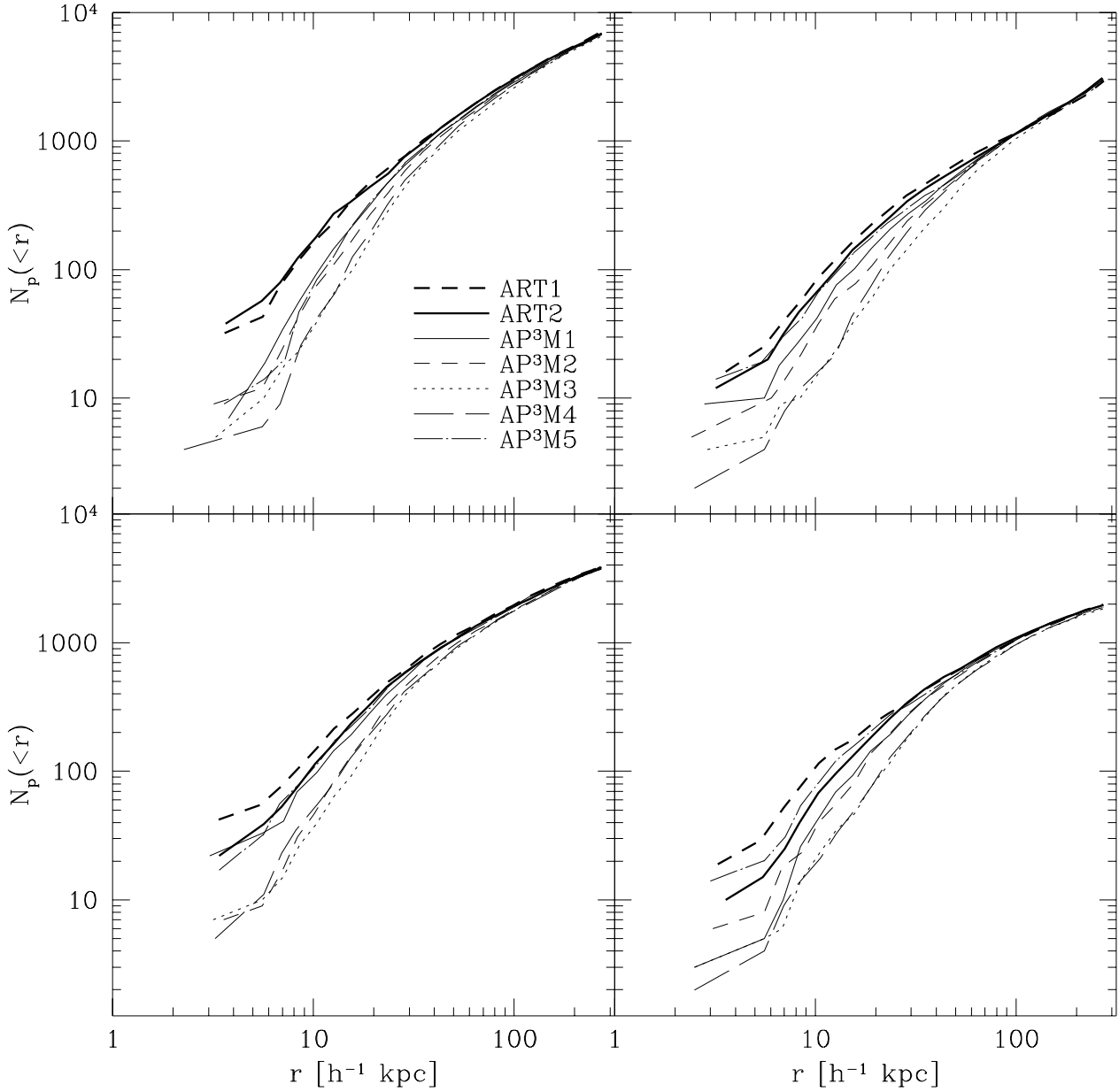


**Figure 13.** Cumulative number of particles within radius  $r$  from the centers of four halos shown in the previous figure.

gued by Splinter et al. (1998) to be the smallest trustworthy scale. At smaller scales the profiles become more noisy due to poorer particle statistics (see Fig. 13).

Nevertheless, there are systematic differences between the runs. The profiles in two ART runs are identical within the errors indicating convergence (we have run an additional simulation with time steps twice smaller than those in the ART1 finding no difference in the density profiles). Among the AP<sup>3</sup>M runs, the profiles of the AP<sup>3</sup>M1 and AP<sup>3</sup>M5 are closer to the density profiles of the ART halos than the rest. The AP<sup>3</sup>M2, AP<sup>3</sup>M3, and AP<sup>3</sup>M4, despite the higher force resolution, exhibit lower densities in the halo cores, the

AP<sup>3</sup>M3 and AP<sup>3</sup>M4 runs being the most deviant. These differences can be seen more clearly in Fig. 13, where we plot the cumulative number of particles (i.e., mass) within radius  $r$  for the halos shown in Fig. 12. The differences between AP<sup>3</sup>M3 and AP<sup>3</sup>M4 and the rest of the runs are apparent up to the radii containing  $\sim 1000$  particles.

These results can be interpreted, if we examine the trend of the central density as a function of the ratio of the number of time steps to the dynamic range of the simulations (see Table 1) shown in Table 4. The ratio is smaller when either the number of steps is smaller or the force resolution is higher. Table 4 shows that agreement in density

**Table 4.** The ratio of number of time steps to the dynamic range of simulations for the high-resolution runs. The number of time steps for the ART runs correspond to the time step on the highest refinement level.

Run	$N_{step}/\text{dyn.range}$
AP <sup>3</sup> M4	0.469
AP <sup>3</sup> M3	0.702
AP <sup>3</sup> M2	0.938
AP <sup>3</sup> M1	1.875
AP <sup>3</sup> M5	3.750
ART2	2.578
ART2	5.156

profiles is observed when this ratio is  $\gtrsim 2$ . This suggests that for a fixed number of time steps, there should be a limit on the force resolution. Conversely, for a given force resolution, there is a lower limit on the required number of time steps. The exact requirements would probably depend on the code type and the integration scheme. For the AP<sup>3</sup>M code our results suggest that the ratio of the number of time steps to the dynamic range should be no less than one. It is interesting that the deviations in the density profiles are similar to and are observed at the same scales as the deviations in the DM correlation function (Fig. 8) suggesting that the correlation function is sensitive to the central density distribution of dark matter halos.

These results are indicative of the sensitivity of the central density distribution in halos to parameters of the numerical simulation. However, due to the limited mass resolution of our test runs, they do not shed light on the density profile debates. The profiles of the ART halos agree well with those of the AP<sup>3</sup>M halos, if the latter are simulated with a sufficiently large number of time steps. But debated differences are at scales of  $\lesssim 0.01R_{\text{vir}}$ , which are not resolved in these simulations. We are currently carrying out a more detailed, higher-resolution study to clarify the issue.

#### 4.6 Shared Particles

We have argued above that particle trajectories may diverge in high-density regions due to their instability to small integration errors. However, despite the instability of its trajectory, we can expect that a bound particle will stay bound to its parent halo. To this end we compare the particle content of individual halos in different runs. We have identified the counterpart halos in different runs as systems that have the largest number of common (or shared) particles. This method is superior to coordinate based methods because due to the phase errors (see § 3.3) one does not expect to find the halos at the exact same position in different runs (this is especially not for small groups of particles).

Fig. 14 shows the percentage of mass that can be found in particle groups that coincide in a specific amount of

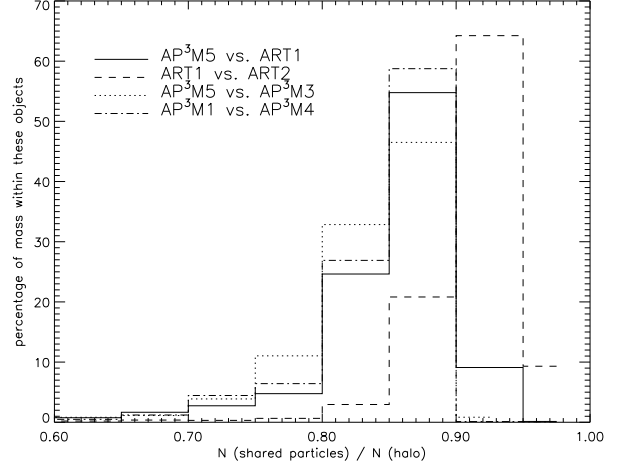


**Figure 14.** Percentage of mass included in halos with a specific amount of shared particles and containing at least 25 particles.

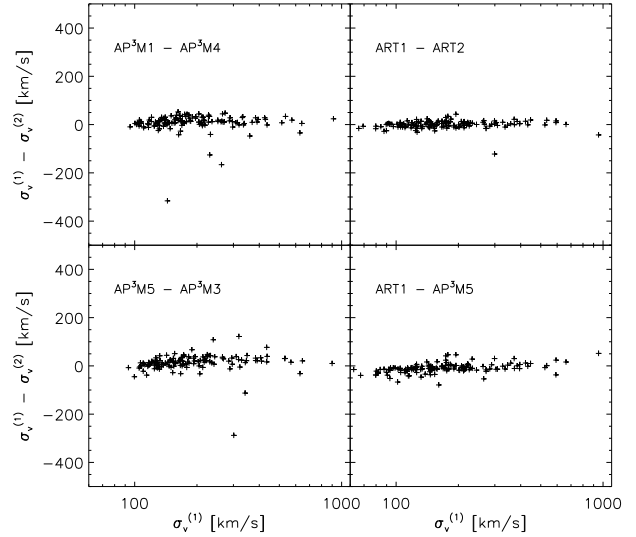


**Figure 15.** Correlation of the velocity dispersions of the same halos identified in two different simulations. Only halos with more than 50 particles are taken into account

shared particles. The figure shows that in all runs most halos have more than 80% of their particles in common. The distributions peak at around 85-90% for all of the comparisons, except ART1 vs. ART2 which peaks at  $\approx 90 - 95\%$ . Even though a direct comparison of particle positions within halos is not a very useful way of comparing different runs, this result shows that the particle content of halos is rather similar.

#### 4.7 Correlation of Velocity Dispersions

In Fig. 15 we compare the velocity dispersions of halos identified in different simulations by the FOF algorithm assuming a minimum particle number of 50 per halo. The figure shows that the velocity dispersions agree reasonably well



with the overall scatter of  $\sim 50 \text{ km s}^{-1}$ . The very few outliers are halos of very different masses identified as the same halo by the FOF algorithm. Small differences in particle distribution may result in the identification of a binary system in one simulation and only a single halo in another simulation, leading to the large differences in velocity dispersions.

The differences between velocity dispersions appear to be independent of halo mass, and although they reach  $\sim 50\%$  for the lowest mass halos, there are no obvious systematic differences between different simulations.

## 5 DISCUSSION AND CONCLUSIONS

We have presented results of a study of resolution effects in dissipationless simulations. As we noted in the introduction, an additional goal of this study was to compare simulations done using two different high-resolution  $N$ -body codes: the AP<sup>3</sup>M and the ART. Our results indicate that both codes produce very similar results at all scales resolved in the presented simulations, given the force resolution and time step are such that convergence is reached within the code type. Our results indicate that numerical effects may be complicated due to a combined effect of mass and force resolution and inaccuracies of the time integration scheme. The precise magnitude of the effects depends on the numerical parameters used and the considered statistics or property of particle distribution.

Particles in dissipationless cosmological simulations are supposed to represent elements of the dark matter distribution in phase space<sup>†</sup>. The smaller the particle number, the larger the volume associated with each of the particles. During the course of evolution, according to Liouville's theorem, the phase-space volume of each element should be preserved. Its shape, however, will be changing. Correspondingly, the eulerian space volume of these elements may shrink (for particles in an overdense collapsing region of space) or expand (for particles in underdense regions). Regardless of its initial shape, each element can be stretched due to the anisotropic nature of the gravitational collapse in cosmological models.

Usually, none of these effects is modelled in cosmological  $N$ -body simulations. The gravitational field of each particle is assumed to be roughly isotropic and therefore the effects of the volume stretch cannot be modelled. These effects are not addressed in the present study, because they can only be studied by widely varying the number of particles at a fixed force resolution and for a fixed time step<sup>‡</sup>, while we have varied the force resolution and time step keeping the number of particles fixed. A large number of particles corresponds to the smaller phase-space associated with each particle and the symmetric particle approximation is more accurate. Convergence studies of the halo density profiles indicate that these effects are small (at least at radii  $\gtrsim 0.02 - 0.05 R_{\text{vir}}$ ). However, this does not mean that they cannot be important for other statistics.

<sup>†</sup> Unless particles are supposed to represent individual galaxies, which is virtually never the case in modern simulations.

<sup>‡</sup> Due to the phase errors discussed below, such a study should also be carried out using the same numerical code.

Nevertheless, we can study other kinds of resolution effects. Normally, softening of interparticle gravitational force should be approximately equal to the spatial size of the phase-space volume element associated with each particle. If the softening is much smaller than this size, the volume elements will behave like particles and two-body scattering is possible. This was indeed observed in some of our high-resolution simulations. This scattering contradicts the collisionless nature of the modelled dark matter and is thus undesirable.

For the mass resolution of our simulations ( $\approx 3.55 \times 10^9 h^{-1} M_{\odot}$ ), scattering was observed in simulations with uniform force resolution of  $\lesssim 3 h^{-1} \text{ kpc}$  and disappears for larger values of resolution. While we find strong scattering for  $\approx 1.4\%$  of the particles, many more may have suffered weaker scattering events during the course of simulation. Indeed, we find indirect evidence that scattering has substantial effect on the particle distribution. In particular, we find that it may noticeably affects the small-scale amplitude of the 2-point correlation function of dark matter, the abundance and mass function of dark matter halos, and the central density distribution of halos. The effect is amplified strongly for simulations in which larger time steps are used. This is because for larger time steps the scattering events severely violate energy conservation. The magnitude of the violation is very sensitive to the time step: the amount of momentum gained by a particle during a scattering event is  $\propto g \Delta t$ , where  $g$  is the acceleration. Therefore, for the same force resolution (which means that the same  $g$  can be achieved), the momentum gain will be proportional to  $\Delta t$ .

The 2-point correlation function of matter and the central density distribution in halos in our runs are affected by these effects at scales as large as  $\approx 15 - 20$  force softenings. Also, the abundance of satellite halos in high-density regions appears to be affected as well. We think that these effects may be due to the following two phenomena. First, if the time step of the simulation is too large for a given force resolution, particle trajectories are not integrated accurately in the highest density regions, where the gradient of potential is the highest. In some sense, particles scatter off the central density peak, and may gain energy when integrated with large time step (see arguments above). The number of simulation time steps per deflection on a scale  $R$  can be estimates as

$$N_{\text{step}} = \frac{R}{v_{100} \Delta t} \approx 7.51 \times 10^{-4} R N_{\text{step}}^{\text{tot}} v_{100}^{-3}, \quad (6)$$

where  $R$  is in kpc,  $\Delta t$  and  $N_{\text{step}}^{\text{tot}}$  is the time step and the total number of time steps of the simulations, and  $v_{100}$  is particle velocity in units of  $100 \text{ km s}^{-1}$ . We have assumed the Einstein-de Sitter universe with the Hubble constant of  $H_0 = 50 \text{ km s}^{-1} \text{ Mpc}^{-1}$ . For high-velocity particles streaming through the centers of massive halos, there may be just a few time steps to integrate the part of trajectory where strong changes in acceleration occur. As illustrated in Fig. 6, this may not be sufficient to ensure energy preservation and may result in an energy gain by particles. This leads to artificial heating and lowers the central density because having acquired energy, particles are not as likely to enter the central region of halo.

The second phenomenon is due to the “graininess” of the potential. Particles in the high-density regions may feel

the discreteness of the density field and suffer scattering. We do find evidence for scattering in the high-density regions in our simulations (see § 3.4). Here, again, the effect may be amplified strongly by the incorrect integration of such scattering. Indeed, run AP<sup>3</sup>M1 ( $N_{\text{step}}^{\text{tot}} = 8000$ ) performs much better than the run AP<sup>3</sup>M4 ( $N_{\text{step}}^{\text{tot}} = 2000$ ), although both runs have the same mass and force resolution.

The two effects described above may operate in combination, although the first effect does not depend on the mass resolution. The second effect should be eliminated for higher mass resolution. Both lead to the artificial heating of particles thereby lowering the central density of halos and possibly ejecting the particles altogether in some cases. Visual comparisons of halos in the AP<sup>3</sup>M3 (the run which performed the worst) and the AP<sup>3</sup>M5 runs shows that AP<sup>3</sup>M3 halos appear “puffier” and more extended than the same halos in the AP<sup>3</sup>M5 or ART runs. Puffier halos may be destroyed more easily by tides in high-density regions which may explain some of the differences seen between the mass functions of halos in different runs.

Our results show that in constant time step high-resolution simulations the total number of time steps must be rather high to ensure good energy conservation. This requirement can become computationally prohibitive in simulations that follow large numbers of particles. In case of the AP<sup>3</sup>M code, it would probably be preferable to use its version in the publicly available code “Hydra” (Couchman et al. 1995) that uses adaptively varied time step.

The conditions for scattering, discussed in § 3.4, occur if the force softening is smaller than the scale  $s$ , which *in units of mean interparticle separation* is

$$\tilde{s} \approx 1.209 \times 10^{-3} \Omega_0^{1/3} \left( \frac{v}{100 \text{ km s}^{-1}} \right)^{-2} \left( \frac{m_p}{10^8 h^{-1} \text{ M}_\odot} \right)^{2/3}, \quad (7)$$

and is considerably smaller than the *local* interparticle separation:  $d_{\text{loc}} = (1 + \delta)^{-1/3}$  (in units of the mean interparticle separation,  $\delta$  is the local particle overdensity). For our simulations  $s \approx 3v_{100}^{-2} h^{-1}$  kpc, where  $v_{100}$  is particle velocity in units of  $100 \text{ km s}^{-1}$ . This means that condition  $\tilde{s} \ll d_{\text{loc}}$  is satisfied everywhere but in the highest density regions:  $\delta \gtrsim 10^4$ . The conditions for strong scattering occur for the slow moving ( $\lesssim 100 \text{ km s}^{-1}$ ) particles in the AP<sup>3</sup>M runs 1 – 4. Such slow moving particles are likely to be present in the low-density regions and in small-mass halos of velocity dispersion  $\sigma_v \lesssim 100 - 200 \text{ km s}^{-1}$ . This may explain our result that halos of mass  $\lesssim (0.5 - 1) \times 10^{12} h^{-1} \text{ M}_\odot$  ( $\sigma_v \lesssim 100 - 150 \text{ km s}^{-1}$ , see Fig. 10) appear to be affected by scattering.

One may question the relevance of these results, given the small size of the simulations and extremely high force resolution. Note, however, that our results would be applicable (save for the presence of very massive clusters) to any  $256^3$ -particle simulation, in which force resolution of considerably smaller than the scale  $\tilde{s}$  is adopted. The simulations with the particle mass and dynamic range not very far from ours, have already been done. For example, all  $256^3$ -particle simulations of  $239.5 h^{-1} \text{ Mpc}$  box presented by Jenkins et al. (1998) satisfy the condition of  $\epsilon < \tilde{s}$  (where  $\tilde{s}$  is estimated using the above equation for  $v_{100} \lesssim 1.5$ ) and have been run using  $< 1600$  time steps. The parameters of the recent “Hubble volume” simulation (Colberg et al. 1998) also satisfy con-

ditions for strong scattering:  $s \approx 1.9 h^{-1} \text{ Mpc}$ , while force resolution of the simulations is  $\epsilon = 100 h^{-1} \text{ kpc}$ . The particle mass of these simulations is  $\approx 2 \times 10^{12} h^{-1} \text{ M}_\odot$ , which means that individual particles represent galaxies rather than a phase-space element. Galaxies form a collisional system so the presence of scattering may be considered as a correct model of the evolution of galaxy clustering. Moreover, the mean interparticle separation in these simulations is  $\approx 2 - 3 h^{-1} \text{ Mpc}$  and thus conditions for scattering may only occur in the underdense regions.

A high-resolution  $256^3$ -particle run was also done recently using the ART code (see, for example, Colín et al. 1999). However, for this simulation ( $m_p = 1.1 \times 10^9 h^{-1} \text{ M}_\odot$ ;  $\Omega_0 = 0.3$ ) the scale of strong scattering is  $s \approx 0.94 v_{100}^{-2} h^{-1} \text{ kpc}$ , while peak resolution is  $\approx 4 h^{-1} \text{ kpc}$ . The time steps for the particles at the refinement level of this resolution corresponds to effective number of time steps of  $\approx 41,000$ . Therefore, for this simulation the strong scattering condition is not satisfied. Moreover, a refinement level  $L$  is introduced in these simulations only if the local overdensity is higher than  $\delta = 5 \times 2^{3(L+1)}$ , or for the highest resolution level  $L = 6$ :  $\delta \approx 10^7$ . For these overdensities, the local interparticle separation is  $\approx 1 h^{-1} \text{ kpc}$ , and two-body interactions are thus unlikely.

To summarize, scattering can be precluded if the choice of force resolution is guided by the scale  $s$ , which, in turn, depends on the mass resolution (particle mass). This conclusion may seem similar to that of Splinter et al. (1998), who concluded that force resolution should not be smaller than the mean interparticle separation. It is, however, quite different in practice: eq. (7) shows that for our box size  $s \approx 1$  in units of mean interparticle separation only for  $m_p \approx 3 \times 10^{12} h^{-1} \text{ M}_\odot$ . For our mass resolution, force softening as small as  $5 - 10 h^{-1} \text{ kpc}$  is justified. This is  $\sim 25 - 50$  times below the mean interparticle separation.

We think that the conclusion of Splinter et al. is (at least in part) due to the interpretation of poor cross-correlation between different simulations on small scales as erroneous evolution in high-resolution runs. Our analysis, presented in § 3, shows that poor cross-correlation is due to phase errors whose major source is cumulative errors due to the inaccuracies of time integration. The trajectories of particles become chaotic in high-density regions and small differences in time integration errors tend to grow quickly.

For this reason it may prove to be very difficult to get rid of this effect by improving the time integration. Therefore, one should keep these errors in mind if a phase sensitive statistic is analyzed. Luckily, most of the commonly used statistics are phase-insensitive and are not affected by such errors. Moreover, the errors are confined to the small-scale high-density regions, and no significant phase errors are present in our simulations if the density field is smoothed on a scale  $\gtrsim 1 h^{-1} \text{ Mpc}$ .

While this is clearly still an error, it has nothing to do with the mass or force resolution and would be present even if both were perfect. This point is clearly demonstrated by the fact that simulations run using two different implementations of the PM code correlate perfectly within the code type but cross-correlate rather poorly when cross-code comparisons are made (see § 3.3). Note that in all of these PM runs, the force resolution is approximately equal to the mean interparticle separation.

The main conclusion of our study is that care must be taken in the choice of force resolution for simulations. If a code with spatially uniform force resolution is used, conditions for strong two-body scattering may exist if the force resolution is smaller than the scale  $s$  discussed above. The presence of scattering itself may not be important (albeit undesirable); the relaxation time for systems, for example, may be much longer than the Hubble time (e.g., Hernquist & Barnes 1990; Huang, Dubinski & Carlberg 1993). Its effects, however, may be greatly amplified if the time step of the simulation is not sufficiently small. In this case, severe violation of energy conservation occurs during each scattering which may lead to artificial injection of energy into the system.

## ACKNOWLEDGEMENTS

AVK and AAK are grateful to the Astrophysikalishes Institut Potsdam (AIP), where this project was initiated, for the hospitality during their visit. We thank referee for useful comments. This work was funded by NSF and NASA grants to NMSU. SG acknowledges support from Deutsche Akademie der Naturforscher Leopoldina with means of the Bundesministerium für Bildung und Forschung grant LPD 1996. Our collaboration has been supported by the NATO grant CRG 972148.

## REFERENCES

- Bhavsar, S.P., & Splinter, R.J. 1996, MNRAS 282, 1461
- Binney, J., & Tremaine, S. 1987, *Galactic Dynamics* (Princeton: Princeton University Press)
- Colberg J.M., White S.D.M., Jenkins A., Pearce F.R., MNRAS submitted ([astro-ph/9711040](#))
- Colberg J.M., et al. 1998, preprint [astro-ph/9808257](#)
- Cole S., Lacey C., MNRAS 281, 716 (1996)
- Coles P., Melott A.L., Shandarin S.F., MNRAS 260, 765 (1993)
- Colín, P., Klypin, A.A., Kravtsov, A.V., & Khokhlov, A.M. 1999, ApJ, in press ([astro-ph/9809202](#))
- Couchman H.P., ApJ 368, L23 (1991)
- Couchman H.P., Thomas, P.A. & Pearce, F.R. ApJ 452, 797 (1995)
- Doroshkevich A.G., Kotok E.V., Novikov I.D., Polyudov A.N. Shandarin S.F. Sigov Yu.S., MNRAS 192, 321 (1980)
- Efstathiou, G., & Eastwood, J.W. 1981, MNRAS 194, 503
- Efstathiou, G., Davis, M., White, S.D.M., & Frenk, C.S. 1985, ApJS 57, 241
- Frenk C.S., et al., The Santa Barbara cluster comparison project, 1998, ApJ submitted ([astro-ph/9906160](#))
- Gelb, J.M. 1992, PhD thesis, MIT
- Hernquist, L., & Barnes, J.E. 1990, ApJ 349, 562
- Hockney R.W., Eastwood J.W., Computer Simulation using Particles, Adam Hilger, Bristol and Philadelphia (1981)
- Hockney R.W., Goel S.P., Eastwood J.W., Chem. Phys. Lett. 21, 589 (1973)
- Huang, S., Dubinski, J., & Carlberg, R.G. 1993, ApJ 404, 73
- Jenkins, A., et al. 1998, ApJ 499, 20
- Klypin A.A., Shandarin, S.F. 1983, MNRAS 204, 891
- Klypin A.A., 1996, in *“Dark Matter in the Universe”*, Proceedings of the International School of Physics “Enrico Fermi”, ed. S. Bonometto et al. ([astro-ph/9605183](#))
- Klypin A.A., Gottlöber S., Kravtsov A.V., Khokhlov A.M., ApJ 516, 530 (1999)
- Kolb, E.W., Chung, D.J.H., & Riotto, A. 1998, preprint [hep-ph/9810361](#)
- Kravtsov A.V., Klypin A.A., Khokhlov A.M., ApJS 111, 73 (1997)
- Kravtsov A.V., Klypin A.A., Bullock, J.S., & Primack, J.R. 1998, ApJ 502, 48
- Kuhlman, B., Melott, A.L., & Shandarin, S.F. 1996, ApJ 470, L41
- Melott, A.L., Splinter, R.J., Shandarin, S.F., & Suto, Y. 1997, ApJ 479, L79
- Moore, B. 1994, Nature 370, 629
- Moore, B., Katz, N., & Lake, G. 1996, ApJ 457, 455
- Moore, B., Quinn, T., Governato, F., Stadel, J., Lake, G. 1999, MNRAS submitted ([astro-ph/9903064](#))
- Navarro, Frenk & White 1997, ApJ 490, 493
- Roszkowski, L., 1999, preprint [hep-ph/9903467](#)
- Splinter R.J., Melott A.L., Shandarin S.F., and Suto Y., ApJ 497, 38 (1998)
- Suisalu I., Saar E., [astro-ph/9511120](#)
- van Kampen, E. 1995, MNRAS 273, 295